Resource

Cell

Saturated Reconstruction of a Volume of Neocortex

Graphical Abstract

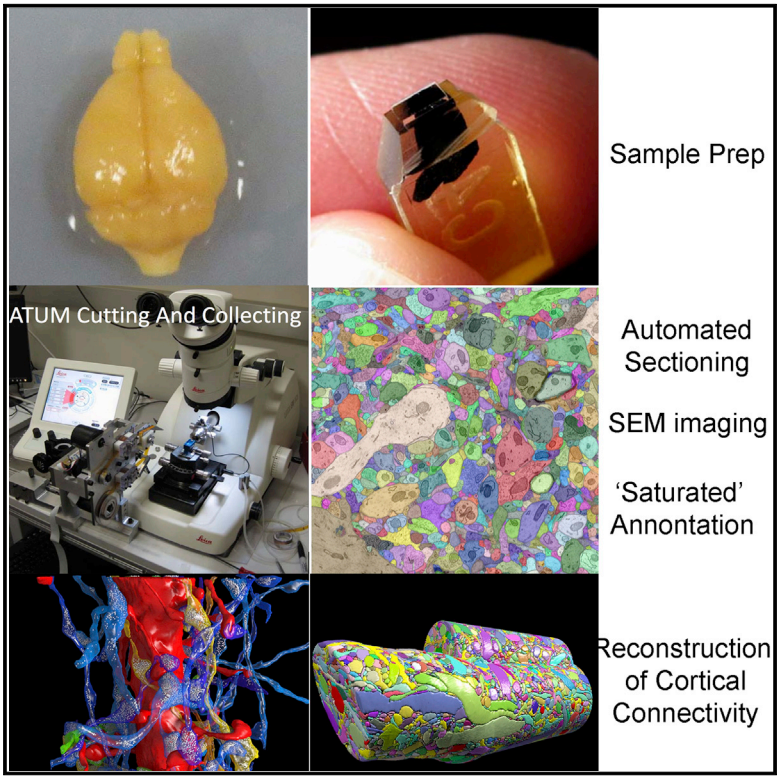

Authors

Narayanan Kasthuri, Kenneth Jeffrey Hayworth, Daniel Raimund Berger, ..., Carey Eldin Priebe, Hanspeter Pfister, Jeff William Lichtman

Correspondence

bobby.kasthuri@gmail.com (N.K.), jeff@mcb.harvard.edu (J.W.L.)

In Brief

Automated technologies probing the structure of neural tissue at nanometer resolution generate a saturated reconstruction of a sub-volume of mouse neocortex, refuting the idea that physical proximity is sufficient to predict excitatory synaptic connectivity.

Highlights

- Tape-based pipeline for electron microscopic reconstruction of brain tissue
- Annotated database of 1,700 synapses from a saturated reconstruction of cortex
- Excitatory axon proximity to dendritic spines not sufficient to predict synapses

Kasthuri et al., 2015, Cell *162*, 648–661
July 30, 2015 ©2015 Elsevier Inc.
http://dx.doi.org/10.1016/j.cell.2015.06.054

CellPress

Cell

Resource

Saturated Reconstruction of a Volume of Neocortex

Narayanan Kasthuri,[1,8,*] Kenneth Jeffrey Hayworth,[1,9] Daniel Raimund Berger,[1,6] Richard Lee Schalek,[1] José Angel Conchello,[1] Seymour Knowles-Barley,[1] Dongil Lee,[1] Amelio Vázquez-Reina,[2] Verena Kaynig,[2] Thouis Raymond Jones,[1,2] Mike Roberts,[2,10] Josh Lyskowski Morgan,[1] Juan Carlos Tapia,[1,11] H. Sebastian Seung,[6,12] William Gray Roncal,[3,13] Joshua Tzvi Vogelstein,[7,14] Randal Burns,[3] Daniel Lewis Sussman,[4] Carey Eldin Priebe,[5] Hanspeter Pfister,[2] and Jeff William Lichtman[1,*]

[1]Department of Molecular and Cellular Biology and Center for Brain Science, Harvard University, Cambridge, MA 02138, USA
[2]School of Engineering and Applied Sciences, Harvard University, Cambridge, MA 02138, USA
[3]Department of Computer Science, Johns Hopkins University, Baltimore, MD 21218-2128, USA
[4]Department of Statistics, Harvard University, Cambridge, MA 02138, USA
[5]Department of Applied Mathematics and Statistics, Johns Hopkins University, Baltimore, MD 21218-2682, USA
[6]Department of Brain and Cognitive Sciences, Massachusetts Institute of Technology, Cambridge, MA 02139, USA
[7]Department of Statistical Science and Neurobiology, Duke University, Durham, NC 27708, USA
[8]Present address: Department of Anatomy and Neurobiology, Boston University School of Medicine, Boston, MA 02118, USA
[9]Present address: Janelia Farm Research Campus, Ashburn, VA 20147, USA
[10]Present address: Department of Computer Science, Stanford University, Stanford, CA 94305, USA
[11]Present address: Department of Neuroscience, Columbia University, New York, NY 10032, USA
[12]Present address: Princeton Neuroscience Institute and Department of Computer Science, Princeton University, Princeton, NJ 08544, USA
[13]Present address: Johns Hopkins University Applied Physics Laboratory, Laurel, MD 20723, USA
[14]Present address: Department of Biomedical Engineering and the Institute for Computational Medicine, Johns Hopkins University, Baltimore, MD 21218-2682, USA
*Correspondence: bobby.kasthuri@gmail.com (N.K.), jeff@mcb.harvard.edu (J.W.L.)
http://dx.doi.org/10.1016/j.cell.2015.06.054

SUMMARY

We describe automated technologies to probe the structure of neural tissue at nanometer resolution and use them to generate a saturated reconstruction of a sub-volume of mouse neocortex in which all cellular objects (axons, dendrites, and glia) and many sub-cellular components (synapses, synaptic vesicles, spines, spine apparati, postsynaptic densities, and mitochondria) are rendered and itemized in a database. We explore these data to study physical properties of brain tissue. For example, by tracing the trajectories of all excitatory axons and noting their juxtapositions, both synaptic and non-synaptic, with every dendritic spine we refute the idea that physical proximity is sufficient to predict synaptic connectivity (the so-called Peters' rule). This online minable database provides general access to the intrinsic complexity of the neocortex and enables further data-driven inquiries.

INTRODUCTION

The cellular organization of the mammalian brain is more complicated than that of any other known biological tissue. As a result, much of the nervous system's fine cellular structure is unexplored. While it has been known for more than a century that a directional network interconnects many kinds of nerve cells (Cajal, 1899), and that this network underlies behaviors (Sherrington, 1906), for the most part, the precise relationships between the brain's many cellular components are not known. Several laboratories are now beginning to generate such data in mammals using electron microscopy (EM). This work has provided new insights into the visual system (Anderson et al., 2011; Helmstaedter et al., 2011; Kim et al., 2014; Briggman et al., 2011; Bock et al., 2011; see also Takemura et al., 2013; Mishchenko et al., 2010). Descriptions of neuronal network structure could also be important if derangements in networks underlie psychiatric or developmental disorders and/or if modifications to these networks store learned information (i.e., memories). Exploring such possibilities may require methods for obtaining detailed synaptic-level connectomic data.

A reconstruction effort on the scale of mammalian brains, however, would be enormously expensive and difficult to justify without assurances that this kind of information would be of value (Marblestone et al., 2013; Plaza et al., 2014; Lichtman et al., 2014). Substantial savings in effort could come if the connectivity of the cerebral cortex could be ascertained without looking at every single synapse. For example, if the overlap of axons and dendrites at light microscope resolution provides sufficient information to infer connectivity (Hill et al., 2012), huge data sets of EM images of cerebral cortex might be superfluous. We thus decided to reconstruct all the connectivity within a very small piece of neocortical tissue (1,500 μm^3 at a resolution allowing identification of every synaptic vesicle) to be in a better position to decide whether or not obtaining complete brain maps at such a fine level of resolution reveals interesting properties that cannot be inferred from either lower resolution or more sparse analyses.

Previous connectomic studies of retina and hippocampus concluded that connectivity was not entirely predictable from the proximity of presynaptic elements to postsynaptic targets (Briggman et al., 2011; Mishchenko et al., 2010; Helmstaedter

CrossMark

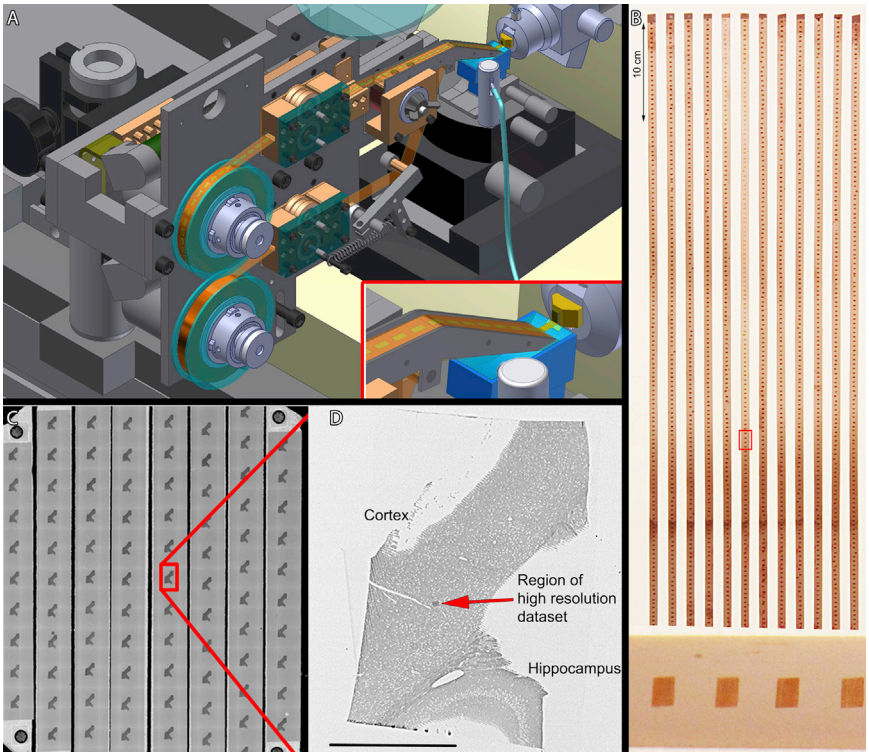

Figure 1. Automatic Tape Collection of Ultrathin Brain Sections

(A) Diagram of the automated tape-collecting ultramicrotome (ATUM). The bottom reel of the ATUM contains a plastic tape that is fed into the knife boat of a diamond knife mounted on a commercial ultramicrotome. The tape is collected on a take up reel (top). (Red inset) Close-up view of the tape conveyor positioned in the knife boat. The diamond knife boat (dark blue) is filled with water (light blue). The diamond knife (green rectangle) is at the opposite end of the knife boat from the taping mechanism. It cuts serial ultrathin sections from tissue embedded in a plastic block. The sections then float on the surface of the water in the knife boat until they adhere to the moving tape (see Movie S1).

(B) ~10 m of Kapton tape with ~2,000 sections collected. Four of the 29-nm sections (red rectangle) are shown at a higher magnification at the bottom of the panel.

(C) The reel of tape is then cut into individual strips and mounted on silicon wafers for poststaining and/or carbon coating. A low-power scanning electron microscopy image of part of a wafer containing 85 brain sections is shown. One of the sections (red rectangle) is shown at a higher magnification in the next panel.

(D) One 29-nm section containing neocortex and hippocampus. The region that was studied at high resolution is the dark-looking box (red arrow). Scale bar, 1 mm.

See also Movie S1.

et al., 2013). We wished to examine this question again but now in neocortex for several reasons. First, a large effort is underway to model and simulate neocortical processing based on stochastic connectivity based on spatial overlap of axons and dendrites (Markram et al., 2012). Second, the retina and the hippocampus (archicortex) are phylogenetically older than neocortex and may have evolved deterministic targeting mechanisms that could explain why overlap is insufficient to predict connectivity in those regions. In neocortex, however, less is known and it remains possible that spatial overlap is sufficient to explain synaptic connections between particular pairs of axons and dendrites. Third, in analyzing our data, we have found significant redundancies in the synaptic connections and wanted to know if these were accidental. For all these reasons, we have attempted to analyze the connectivity of each of many axons and dendrites by looking at not only the synapses each axon establishes but also the occurrences when axons and dendrites get close with potential postsynaptic targets but do not establish synapses.

Even for such a small volume, however, we found considerable technical challenges standing in the way of doing such an analysis. After "saturating" the segmentation of a sub-region in the middle of the imaged volume in which all intracellular space was assigned to one or another cellular entity, we then needed to catalog all the connectivity and structural information into a minable database before analyses. Surprisingly, analysis of the connectomic data turned out to be even more challenging than creating the image data or annotating it.

This "omics" approach provided a wealth of data for potential analysis. Here, we investigate aspects of the connectivity of excitatory axons and find interesting patterns that would have been difficult to detect with lower resolution methods. To assist readers who wish to examine the data in detail, we serve out the images and their segmentations and annotated databases that link to the image data, as well as all the software we developed for the display and analysis (described herein http://openconnecto.me/Kasthurietal2014/).

RESULTS

The results are divided into two parts. We first describe the technical approaches for acquiring and analyzing this data and then turn to some of the biological findings.

TECHNICAL DETAILS

Collecting Serial Brain Tissue Sections on Tape

We built an automatic tape-collecting ultramicrotome (ATUM) that retrieves brain sections from the water boat of a diamond knife immediately as they are cut via a continuous submerged conveyor belt (Figure 1A; Movie S1). The tape's pulling motion and its adhesiveness cause the caught sections to lie flat on the tape's surface (Figure 1A, inset). To generate the cerebral cortex image dataset in this paper, we collected 2,250 29-nm coronal brain slices (each section ~1 mm^2, total volume 0.13 mm^3) from somatosensory cortex of a young adult mouse on ~6.5 m of Kapton tape (Figure 1B). We generated 1,000 sections per 24 hr. We chose 29 nm as section thickness in order to trace the finest neuronal wires (Mishchenko, 2009), and with a

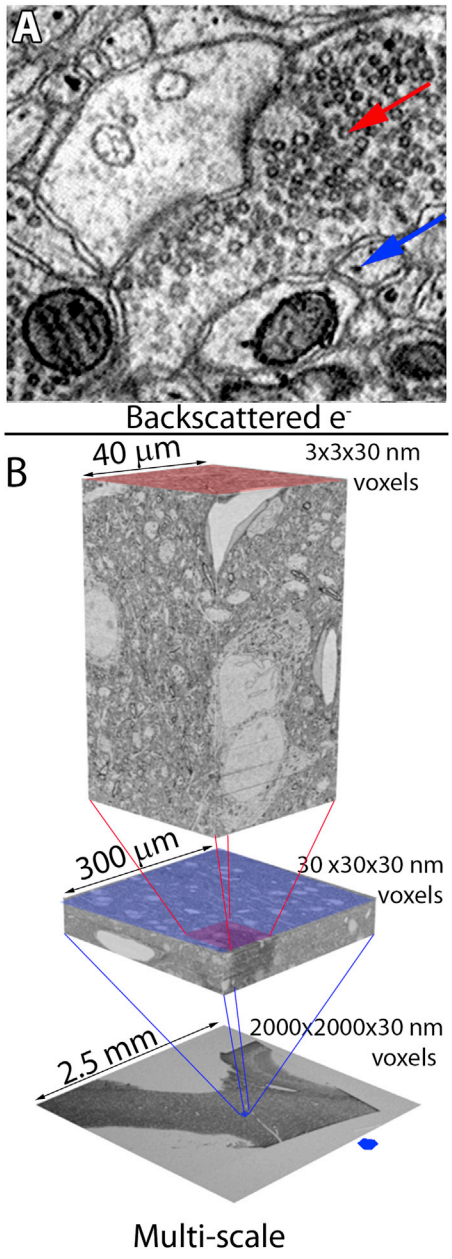

Figure 2. Imaging Brain Sections on Tape

(A) A section of somatosensory neocortex imaged in a scanning electron microscope. The red arrow shows synaptic vesicles. The blue arrow shows a strongly labeled membranous tube found in unmyelinated axons.

(B) The strategy for placing high-resolution images in a larger anatomical context by re-imaging sections at multiple resolutions. The sections used for all of the subsequent analysis in this paper are ~2.5 mm^2.

See also Figure S1 and Movies S2, S3, S4, and S5.

sharp knife we have successfully sectioned >10,000 sections from a small block without missing a cut and importantly manual segmentation is nearly flawless at this thickness (see below). Following section collection, the tape was cut into strips and placed on silicon wafers that were then photographed (Figure 1C). The wafer image was used to map the positions of the sections on the wafer for automated EM (Hayworth et al., 2014). Once mapped, the wafers constitute an ultrathin section library for repeated imaging of the sections at a range of resolutions (Figures 1D and 2; Movies S2, S3, S4, and S5).

Image Acquisition

Sections were imaged with a scanning electron microscope using backscattered electron detection (9–10 keV incident electron energy), which had sufficient resolution and contrast to detect individual synaptic vesicles (red arrows, Figure 2A). In this study, reduced osmium tetroxide-thiocarbohydrazide (TCH)-osmium (ROTO) was used as stain (Friedman and Ellisman, 1981; Tapia et al., 2012). The ROTO stain highlights a tubular organelle coursing through most unmyelinated axons, aiding in reconstruction of fine processes (blue arrows, Figure 2A) (Sinha et al., 2013; Movies S4 and S5). The plasma membranes with this staining protocol were 6–8 nm in width. We acquired high-resolution images with 3-nm pixels, ensuring that membrane boundaries would be oversampled for easier reconstruction. The same sample was imaged at lower resolutions (30 or 2,000 nm) to rapidly acquire images of larger tissue volumes (Figure 2B). Image acquisition scan rate was 1 M pixels per s. Time is also spent moving the stage from one section to another and automatic focusing each successive section, roughly halving the overall throughput.

Speed-up can be achieved in several ways, including imaging different wafers in parallel on multiple microscopes, use of secondary electron detection (with 1.5–3 keV incident electron energy and speeds of up to 40 M pixels per s; Figure S1A), and by imaging in a new microscope that parallelizes imaging by use of multiple scanning beams (Eberle et al., 2015; Figure S1B).

Generating a Multi-Scale Dataset from Cerebral Cortex

We created a multi-scale digital volume in order to provide tissue context surrounding the region in which we did circuit reconstruction. We first imaged all the sections in their entirety at low resolution (2 μm/pixel). We also imaged a sub-volume (a radial strip of cerebral cortex extending from the pia to white matter, 500 μm wide and 1 mm long) at 29 nm/pixel and finally we imaged an ~80,000 μm^3 box (40 × 40 × 50 μm^3) that transected the apical dendritic bundle of a cortical mini-column (Krieger et al., 2007) at high resolution (3 nm/pixel) (Figure 2B; Movies S4 and S5).

VAST

A manual tool to segment neuronal processes in the image data: we developed a computer-assisted manual space-filling segmentation and annotation program ("VAST," http://openconnecto.me/Kasthurietal2014/Code/VAST/). VAST allowed us to work with EM images online, avoiding the need for their local storage, to "color" the images in at multiple scales of resolution, to organize the results in a flexible annotation framework, to export results for 3D visualization and analysis, and to do these tasks without being limited by working memory. We tested the accuracy of this manual tracing approach, by analyzing saturated segmentations in which every membrane-bound object in every section was colored in. We used

a Matlab script (http://openconnecto.me/Kasthurietal2014/Code/findOrphans) to find "orphans" (i.e., segmented objects that were not connected to parent axons and dendrites; see the Supplemental Experimental Procedures for details). The analysis found that in a ~500 μm^3 cylinder surrounding an apical dendrite (see below), there were no axonal or dendritic orphans in the volume, which included a total of 568 spines and 601 terminal axon branches. With the VAST manual reconstructions, miswiring errors (e.g., connecting the spine head or terminal axon varicosity to the wrong parent process) were also apparently rare because there was substantial agreement between two experienced tracers working independently in the assignment of the finest processes to their parent dendrites or axons (spine necks >99%; 565/568 agreement and axonal terminal branches >99%; 598/601 agreement). In the six cases of disagreement, the two tracers reached consensus once they compared results, meaning there were no places in which the axonal and dendritic data were actually ambiguous. However, for the astrocytic cytoplasm (Figure 3J), there were many glial fragments for which experts could not agree on how they were connected.

RhoANA

Suite of automatic tracing tools: based on the tracing, we found 6.4 profiles per μm^2 in a section and estimated that in the 64,000 um^3 high-resolution volume there are 13.7 million cell profiles in its 1,850 sections. Experienced tracers require about 15 min to trace the ~200 cell profiles in 1 μm^3 so about two people-years of 24/7 tracing would be required to segment out all the profiles in this volume. We therefore developed ways to generate more rapid and automated segmentation of neural processes (details and software are available at http://www.rhoana.org/). To aid this effort, we manually traced all of the cellular objects in several small volumes (~150 μm^3) and used this "stained glass" segmented image data (Figure 3B) to train automated reconstruction methods (Fusion: Vazquez-Reina et al., 2011; Kaynig et al., 2013; GALA: Nunez-Iglesias et al., 2014). Based on this training, we produced automated segmentations of all the cellular processes within a high-resolution volume with dimensions of 30.7 × 30.7 × 33.7 μm (via the RhoANA pipeline using random forest membrane probabilities and graph-cut segmentations with the Fusion segmentation algorithm). In a sub-volume of the cube centered on the "red" neuron's apical dendrite (see below), we produced a different segmentation (via RhoANA using the Maxout deep-learning convolutional neural network for membrane probabilities and the GALA segment agglomeration algorithm). These automatically segmented volumes are available at http://openconnecto.me/Kasthurietal2014/data/automatic_segmentation (Figure 3C; Movie S7).

We found that although fully automated methods are improving rapidly, they are still only first passes and require human assistance to correct merge and split errors. In single images, we found that 92.6% of the pixels or 87.6% (of 92,747) of the profiles were correctly segmented with a fully automated segmentation algorithm (RhoANA with Maxout and GALA; Figures S2A and S2B). However, despite the appearance of largely correct two-dimensional data, when we analyzed cellular profiles in three dimensions, we estimated the need for ~0.9 split operations (to correct inappropriate mergers) and 5.8 merge operations (to correct splits) per μm^3 (Figure S2C; Movie S8). We did these corrections for a sub-volume of the full segmented dataset (cylinder 3; see below), with a newly developed tool for computer-assisted editing and rendering (Mojo and an online version for this tool "Dojo"; Haehn et al., 2014; available at http://www.rhoana.org/). The most important metric for automated reconstruction is the accuracy of the resulting connectivity matrix, but we concluded that at present it is premature to generate fully automated connectivity matrices.

Biological Analysis of the Serial EM Images of Cerebral Cortex

In the medium resolution volume, we identified neuronal somata in order to locate the cortical layer boundaries (Figure 3A) and reconstructed the shapes of a subset of cells running in a cortical mini-column (Figure 3A; Movie S6). Most (~70%, 21/30) of these cells were pyramidal and the rest fell into several different categories, including putative interneurons, atypical excitatory cells, and glial cells. We then fully annotated a sub-volume of somatosensory cortex within this same volume (Movie S9; http://openconnecto.me/Kasthurietal2014/data/segments). Building on work done previously in the hippocampus (Mishchenko et al., 2010; Stepanyants and Chklovskii, 2005), we itemized all the neuronal and non-neuronal cells in three cylindrical volumes that encompass apical dendrite segments of two cortical pyramidal cells, including their spines (Movie S10). We selected these particular apical dendrites because they ran very close to each other (see pink arrow in Figures 3A and 3D) and originated from nearby neuronal somata (in upper layer 6; red and green arrows in Figures 3A and 3D). Thus, they appeared to be in the same mini-column and perhaps participated in the same neural processing unit (Mountcastle, 1997). The three cylinder site was in layer 5, 100 μm and 135 μm superficial to the pseudo-colored "red" and "green" neuronal somata, respectively. Cross-sections of the annotations of two cylinders are shown in Figures 3B and 3D; reconstruction of the three cylinders is shown in Figure 3E; and the location of all three cylinders in the full volume is shown with pink arrows in Figures 3A, 3D, and 3O. These three slightly overlapping ~600 μm^3 cylinders, two of which (cylinders 1 and 3) are centered on the "red" neuron's apical dendrite and one (cylinder 2) on the "green" apical dendrite, provided a total reconstructed volume of 1,500 μm^3. In cylinder 3, rather than tracing the objects manually, we edited the computer-segmented data (Figure 3C). All of the 193 dendrites in this volume were traced out into the surrounding high-resolution cube, and some were traced onto the medium resolution data to locate somata (n = 30; Figure 3O).

Parts List: 3 Cylinder Volume

The 1,500 μm^3 3 cylinder volume contains parts of many cells (Movies S10 and S11) and of a variety of types (Figures 3E–3N; Movie S11), including 193 dendrites, 92% spiny, the rest relatively smooth (Figures 3K and 3N), and 1,407 unmyelinated axons. Based on synapse appearance, 93% of the axons are excitatory (Figure 3I), and most of the remainder are inhibitory (Figure 3L). A few axons (5; ~0.5%), despite possessing vesicle-filled varicosities, did not establish classic close synaptic

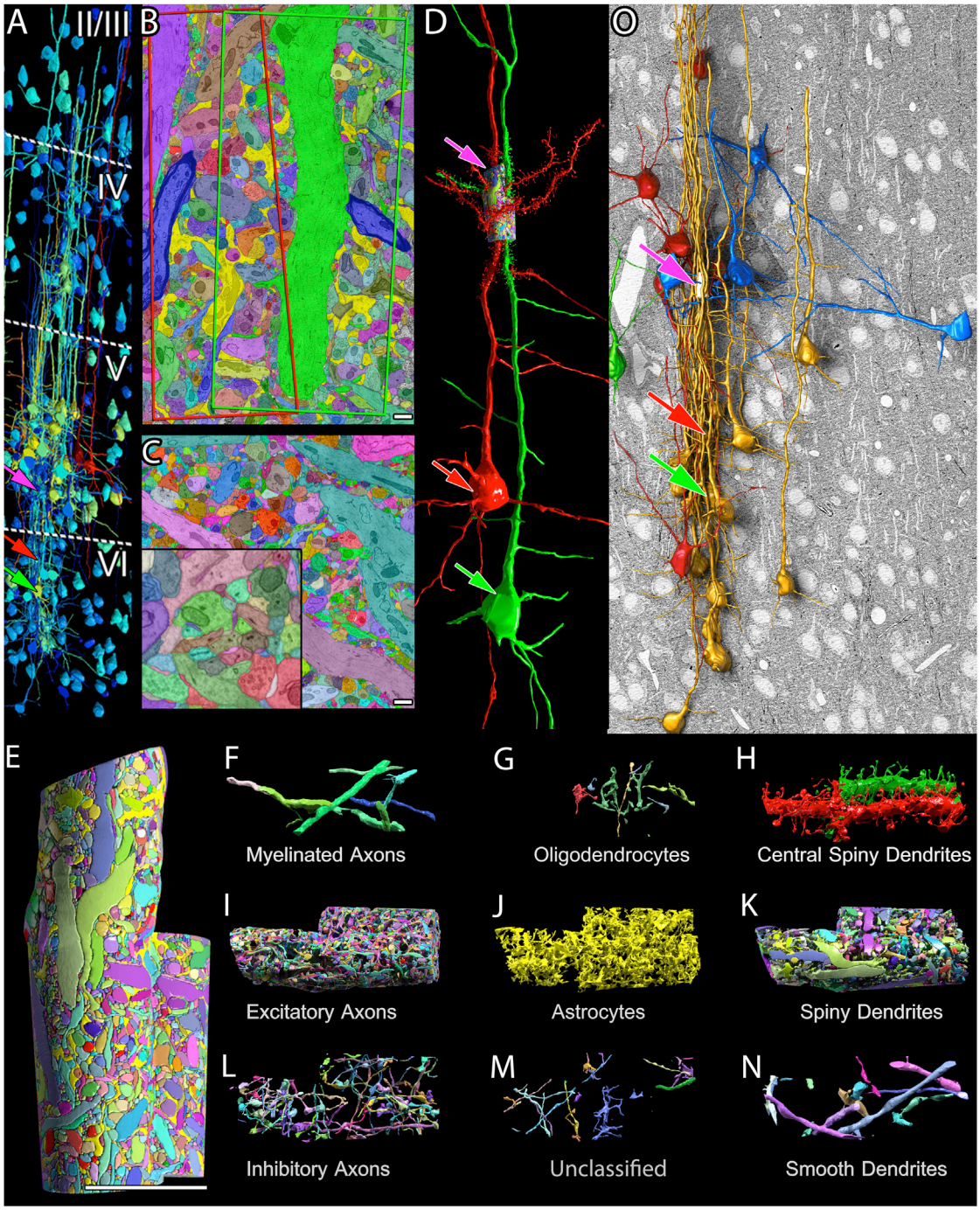

Figure 3. Multi-Scale Reconstruction in Neocortex

(A) Cortical neuronal somata reconstruction to aid in cortical layer boundaries (dotted lines) based on cell number and size. Large neurons are labeled red; intermediate ones are labeled yellow; and small ones are labeled blue. The site of the saturated segmentation is in layer V (pink arrow). These two layer VI pyramidal cell somata (red and green arrows) give rise to the apical dendrites that form the core of the saturated cylinders.

(B) A single section of the manually saturated reconstruction of the high-resolution data. The borders of the cylinders encompassing the "red" and "green" apical dendrites are outlined in this section as red and green quadrilaterals. This section runs through the center of the "green" apical dendrite (full data stack in Movie S9).

(C) A single section of a fully automated saturated reconstruction of the high-resolution data (full data stack in Movie S7). Higher magnification view (lower left inset) shows 2D merge and split errors (for 3D errors see; Figure S1).

(D) The two pyramidal cells (red and green arrows) whose apical dendrites lie in the centers of the saturated reconstructions. Dendritic spines reconstructed in the high-resolution image stack only.

(legend continued on next page)

junctions with postsynaptic cells. In total, there were 1,700 synapses at a density of one synapse per 1.13 μm^3 (Table S1). We also observed astrocytic processes (Figure 3J), myelinated axons (Figure 3F), oligodendrocyte processes (Figure 3G), and about 20 entities that we could not as easily classify (Figure 3M). Neuronal processes (axons and dendrites) occupy 92% of the cellular volume with glial processes, occupying much of the remaining 8% (Movies S9 and S10). The non-cellular (extracellular) space accounts for 6% of the total volume, less than half the extracellular space estimates from living brains, probably because of fixation-induced swelling (Vanharreveld et al., 1965).

The ~7-fold disparity between the number of axons and dendrites (1,407 versus 193) likely reflects a real difference in the numbers of pre- and postsynaptic cells that send processes into the volume. We analyzed the shape of the 660 excitatory axons that entered cylinder 1 and found that only three of them (0.5%) established branches that were non-terminal within the volume (Figure S3). To estimate the number of axons that branched outside the cylinders and sent more than one branch in, we analyzed axonal arbors from light microscopy reconstructions of mouse neocortical pyramidal neurons (NeuroMorpho.org; see the Methods) by superimposing them on the cylindrical volumes at random locations. The result of this analysis argues that only ~8 of the 1,308 excitatory axons (< 1%) in the volume are likely to be branches originating from the same parent neuron. Also, the dendrites in the cylinder only rarely originated from the same neuron: we found two dendritic shafts in cylinder 1 that were from the same neuron (out of 100). Presumably, therefore, axons extend into a 7-fold greater volume than dendrites, on average. The ~1,600 different neurons within this small region of mammalian brain (several billionths of the volume of a whole brain) is more than five times as many neurons as are contained within the entire nervous system of a *Caenorhabditis elegans* (White et al., 1986).

Synapses in the Reconstructed Volume

We created a spreadsheet of the 1,700 synaptic connections in the volume, providing the location of each, its pre- and postsynaptic partners, and a wide variety of other information (Table S1; http://openconnecto.me/Kasthurietal2014/view/highResAnnotated; http://openconnecto.me/Kasthurietal2014/data/synapses).

The spreadsheet shows that the connectivity is highly skewed toward excitatory elements: 92% (177/193) of the dendrites are spiny and purportedly excitatory (Figure 3K; DeFelipe and Fariñas, 1992), and 93% (1,308/1,407) of the axons are excitatory. Looking at each presynaptic varicosity, we found that 95% (1,610/1,700) of them also meet the criteria for being excitatory. Each excitatory axon establishes slightly more synapses in the volume than each inhibitory axon (~1.2 synapses/excitatory axon versus ~0.9 synapses/inhibitory). The excitatory-to-inhibitory-synapse ratio (van Vreeswijk and Sompolinsky, 1996; Wehr and Zador, 2003) is 20.2 for the dendrites of excitatory neurons (1,494 excitatory synapses versus 74 inhibitory synapses), whereas the ratio is only 9.7 (116 excitatory synapses and 12 inhibitory synapses) for the input to inhibitory dendrites. These ratios are in line with what has been described in hippocampal studies (Gulyás et al., 1999; Megías et al., 2001).

Most (71%; n = 1,207/1,700) of the synapses in the volume derive from varicosities along axons (en passant synapses), and the rest are at the end of short branches (terminal synapses). 18% of excitatory, and 43% of the inhibitory, axonal varicosities are presynaptic to multiple partners (Figure 4A). Multi-synaptic excitatory varicosities were previously described in the hippocampus (Chicurel and Harris, 1992; Popov and Stewart, 2009). The most extreme example in this dataset is a large excitatory en passant bouton innervating five different postsynaptic targets (Figure 4B). Tracing ten randomly chosen axons (with 78 varicosities) into the larger surrounding volume showed all but one axon had at least one multi-synaptic varicosity, suggesting that axons in general establish both mono- and multi-synaptic varicosities. Excitatory axons establish synapses mostly on spines (94%; n = 1,406/1,700), and inhibitory axons establish mostly on shafts (81%, n = 70/86). A few (1%; n = 7) of the unmyelinated axons, despite having vesicle-filled varicosities, do not make traditional close synaptic contacts with any target cell within the volume (listed as "2" in column 12 in Table S1). Some of these axons have relatively large vesicles that match the description of cortical aminergic axons (see, for example, http://openconnecto.me/Kasthurietal2014/view/bigVesicles) (Smiley and Goldman-Rakic, 1993). We also notice that glial processes associate with synapses in an uneven way (Figure 3J; Movies S9 and S10): ~50% of synapses were not adjacent to any glial process.

We did not find evidence of electrical connections in the three cylinder volume. Gap junction proteins are seen in inhibitory neurons in layers 4 and 6, but not so much in layer 5, where this study was carried out (Deans et al., 2007).

Synaptic Vesicles

In cylinder 1, we identified the location of each synaptic vesicle at 774 synapses (Figures 4A, 4B, 5A, and 5B; Table S1; http://openconnecto.me/Kasthurietal2014/view/highResAnnotated; http://openconnecto.me/Kasthurietal2014/data/vesicles). The counts were similar (±4.6%) when two expert tracers independently counted the same synapses, and they likely reflect the actual number per synapses (Figure S4). The number of vesicles per synaptic varicosity range from 2 to 1,366 for varicosities with one postsynaptic target (mean = 153 ± 127), with significantly greater numbers of vesicles at multi-synaptic varicosities (mean = 200 ± 173; Wilcoxon rank-sum test; p = 0.0005). The

(E) The saturated reconstruction volume.

(F–N) The "parts list" of the saturated volume.

(O) Reconstruction of 30 dendrites contained within cylinder 1 (pink arrow) that were traced back to their cell bodies. These dendrites were predominantly apical dendrites of pyramidal cells (gold), several basal dendrites of pyramidal cells (blue), and in one case both a branch of the apical and a basal dendrite branch of the same pyramidal cell entered the volume (green) and a small number of non-pyramidal cell dendrites (red). The somata of the red and green apical dendrites that lie at the centers of saturated reconstruction are shown at red and green arrows. Scale bars, 1 μm for (B) and (C) and 7 μm for (E).

See also Figures S2 and S3 and Movies S6, S7, S8, S9, S10, and S11.

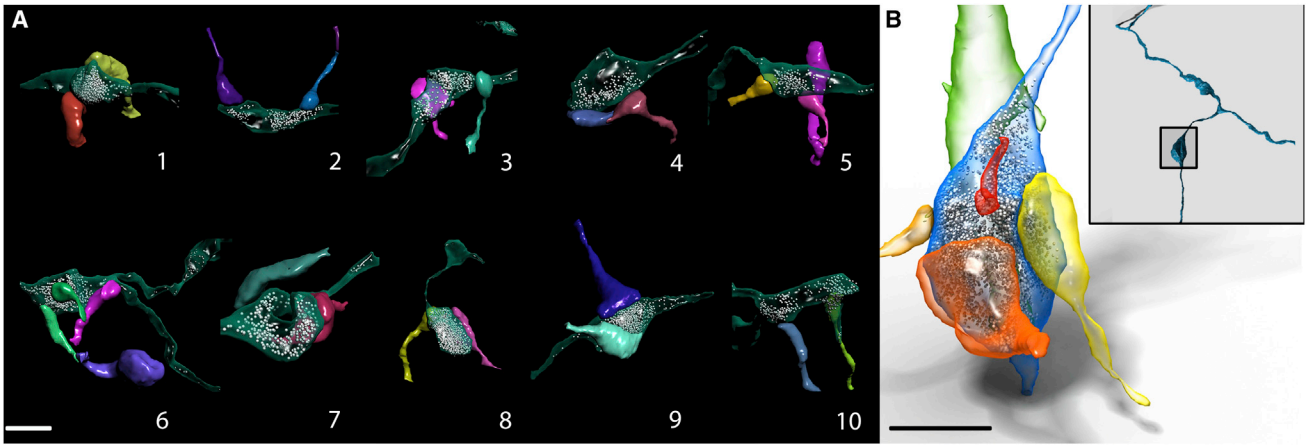

Figure 4. Multi-Synaptic Varicosities Are Commonplace in the Reconstructed Volume of Neocortex

(A) Ten axonal varicosities, which were presynaptic to multiple dendritic spines, are shown. In most cases a single large cluster of vesicles served the multiple synapses. In some cases two spines from the same dendrite were postsynaptic to the same varicosity (e.g., the two purple spines in #5).

(B) An axonal varicosity (blue) that was presynaptic to four dendritic spines (red, orange, yellow, and gold) and one dendritic shaft (green). Inset shows that this was an en passant varicosity of an axon. Scale bar, 1 μm in (A) and (B).

number of vesicles is not significantly different in excitatory and inhibitory synapses.

Mitochondria Size and Density in Different Cells

We also identified 607 mitochondria in cylinder 1 with a density of ~1/μm^3 (Figure 5C; mitochondrial dataset available http://openconnecto.me/Kasthurietal2014/view/highResAnnotated and http://openconnecto.me/Kasthurietal2014/data/mitochondria). Mitochondria occupy twice as much volume in inhibitory dendrites than in excitatory dendrites, perhaps related to the metabolic demands associated with greater levels of activity (Beierlein et al., 2003). In addition, mitochondria are present in axonal varicosities, most typically varicosities that had large numbers of vesicles (Table S1). Only very rarely (n = 3/1,425) do mitochondria reside in dendritic spines, a surprising result given the fact that mitochondria are transported to spines with intense stimulation (Li et al., 2004). Among the three mitochondria that enter spines, two were continuations of mitochondria in the parent dendrite (http://openconnecto.me/Kasthurietal2014/view/spineMito1; http://openconnecto.me/Kasthurietal2014/view/spineMito2; http://openconnecto.me/Kasthurietal2014/view/spineMito3).

Spine Numbers and Sizes

We itemized 1,425 dendritic spines in the 3 cylinder volume. They occupy ~9% percent of the intracellular space. Although each of the three cylinders was constructed around a single apical dendrite to capture nearly all of its spines, there were many more spines from other dendrites that invaded this territory, i.e., the central "red" dendrite contributes only 12%; n = 77/628 of the spines in cylinder 1. Furthermore, the central dendrite's spines were completely intermingled with the spines of other dendrites (see Figure 7A; Movie S12).

In general, spines appear more densely packed (~51 spines per 10 μm dendritic length for the red dendrite in cylinder 1) and often of greater length (mean ~1.8 ± 0.6 μm and longest ~3.8 μm; n = 77) than expected in mouse cortex based on previous reports (Benavides-Piccione et al., 2002). Perhaps this is a consequence of the saturated method of reconstruction, where no spine could be overlooked. The long neck lengths could mean that some of these spines are electrically invisible to the soma (Araya et al., 2006). Larger spine volumes were positively correlated with spine apparati ($r = 0.36$; $p < 0.000001$), larger postsynaptic densities ($r = 0.77$; $p < 0.000001$), larger numbers of presynaptic vesicles ($r = 0.58$; $p < 0.000001$), and presynaptic mitochondria ($r = 0.141$; $p = 0.007$).

Approximately 5% (39/780) of spines belonging to the central dendrite were not innervated by an axon. They appeared longer and thinner than spines that were innervated and often did not terminate in "heads" (Figure S5). These are termed filopodia (Purpura, 1975). Individual filopodia occupied less volume (0.03 ± 0.02 μm^3) than innervated spines (0.10 ± 0.08 μm^3) and only ~30% of them have spine apparati versus 60% of innervated spines.

Connectivity Patterns of Excitatory Axons

We examined excitatory axonal input to dendritic spines that account for three-quarters of the synapses (n = 1,286/1,700) in the 3 cylinder volume and quickly found by mining the data in the synapse spread sheet (Table S1) a potential anatomical correlate of the physiological finding that different excitatory axons can have strikingly different strength connections with the same dendrite (Markram et al., 1998; Song et al., 2005). There were many instances in which the same axon innervated the same dendrite at multiple different spines. Such multiple contacts have been described in the hippocampus (Chicurel and Harris, 1992) and inferred from light microscopy of cortex (Markram et al., 1997). In cylinder 1, the 77 excitatory spine synapses onto its central (red) apical dendrite came from only 63 different axons because eight axons innervated two spines each and three axons innervated three spines (Movie S13). In cylinder 2, 12 of a total of 84 axons innervated two spines of the green dendrite, accounting for 22% of that dendrite's spines. Such multiple contacts were not restricted to apical dendrites because the most extreme example was an axon that innervated

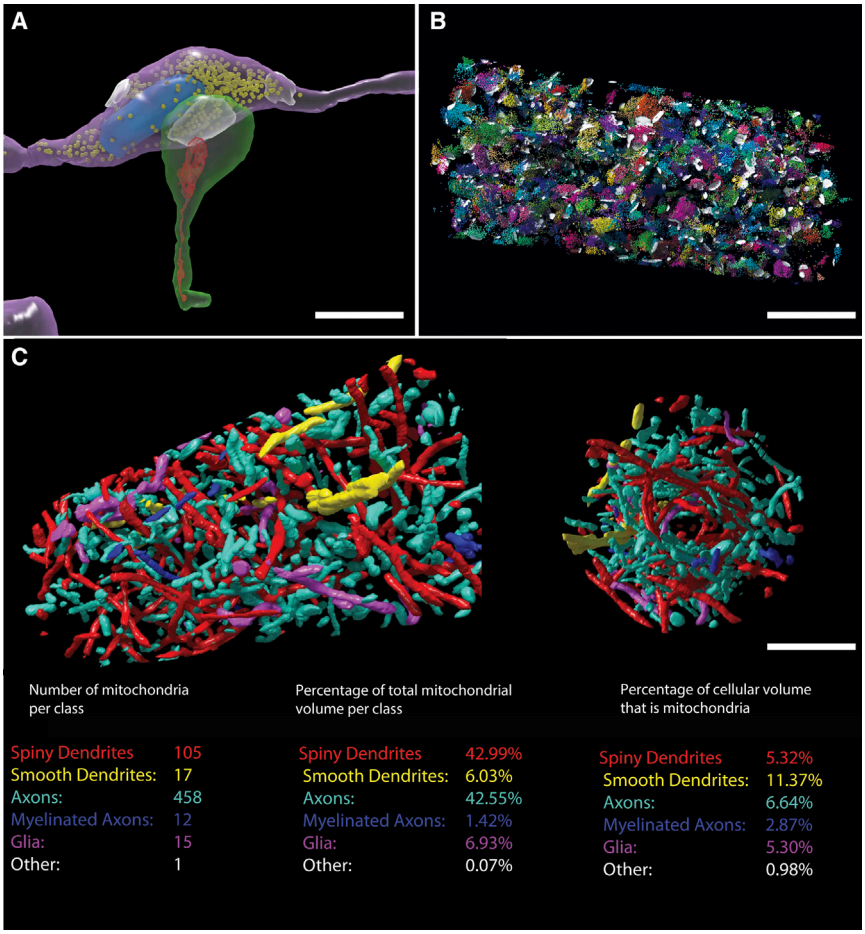

Figure 5. Reconstruction of Subcellular Organelles

(A) A reconstruction of a single synapse showing the innervating excitatory axon and its en passant varicosity (purple), postsynaptic dendritic spine (green), synaptic vesicles (yellow), a presynaptic mitochondrion (blue), the postsynaptic density (white), and spine apparatus (red).

(B) All of the synaptic vesicles in cylinder 1 (n = 162,259) and their corresponding postsynaptic densities (white) are shown. Vesicles with the same color belong to the same axon (full data at http://openconnecto.me/Kasthurietal2014/view/highResAnnotated).

(C) All of the mitochondria (n = 635) contained in cylinder 1 from side view of the cylinder (left) and end-on view (right). Three tables show mitochondrial metrics for cell and process types. Colors of mitochondria in the rendering refer to the classes listed. Scale bars, 1 μm for (A), 7 μm for (B), and 3 μm for (C).

See also Figure S4.

five different spines of a basal pyramidal dendrite (Figure 6). The spines innervated by the same axon were not by rule adjacent either in terms of the location of the spine heads or their origins from the dendritic shaft (Figure 6). In cylinder 1 there were 34 instances in which an axon established synapses on two spines of the same dendrite, 4 instances in which an axon innervated three spines on the same dendrite, and the 1 instance of five just mentioned. Therefore, 46 synapses were "redundant" in the sense that these synapses replicated synaptic connections that were already established by a different synapse of the same axon on the same target cell. For all spines in cylinders 1–3, we counted 97 redundant synapses. However, given the shape of the volume, only the red and green dendrites had all their spines assayed, and thus the measured redundancy almost certainly underestimates the actual amount.

Next, we consider potential reasons for why multiple spine synapses between an axon and a dendrite exist. One idea is that, by virtue of having substantially more branches or a more convoluted path through the volume, some axons have a greater opportunity to establish multiple synapses with the same dendrite than simpler axons. However, there was only a weak correlation between the total length of excitatory axons that crossed through cylinder 1 and the number of synapses they established with its central dendrite (n = 63 axons, 77 synapses; correlation = 0.16; Figure S6A). Alternatively, some axons may have a strong affinity to run near the spines of particular dendrites. We therefore looked at the trajectory of each excitatory axon in greater detail to see if we could discover any differences between the axons that innervated the central ("red") dendrite in cylinder 1 and a cohort of excitatory axons that did not innervate the central dendrite in the cylinder but at least passed immediately adjacent to at least one of its spines (contacts we call "touches," see the Methods for details). Many axons touched each spine (8.9 ± 4.3 excitatory axons touched each spine), but in almost all cases (~99%) only one excitatory axon innervated each (Figure 7B; Movie S14; http://openconnecto.me/Kasthurietal2014/data/touchSynapse). The analysis of axons making touches and those that innervated the central dendrite argues against the idea that the trajectory axons predict their synaptic connectivity. First, for the 77 dendritic spines of the central dendrite in cylinder 1, we found little correlation (correlation coefficient = 0.0001) between the number of these spines that an excitatory axon touches versus the number of synapses it establishes on these spines, as would be expected if synapse probability is just related to the number of opportunities based on proximity to spines (Figure S6B). Second, we found no evidence to support the idea that axons that established the synapses with the central dendrite grew in closer proximity to that dendrite than the axons that touched but did not establish synapses. We compared the length of axons that entered the cylinder and touched a spine of the central dendrite without establishing any synapses with it to the lengths of axons that established synapses with the central dendrite. The axons that touched, but did not establish synapses with the central dendrite, were on average slightly longer in the volume than the axons that established

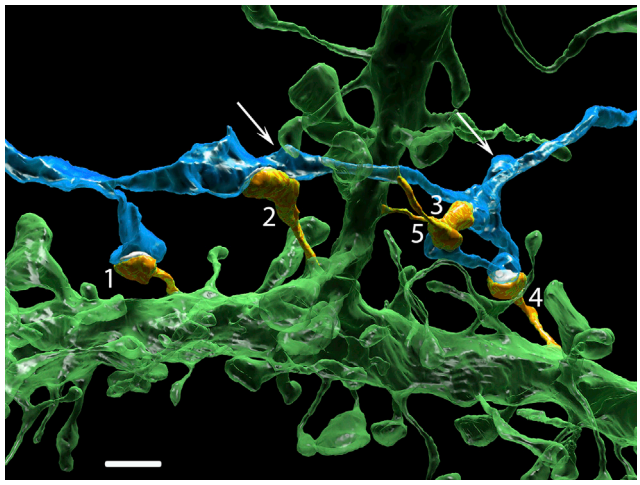

Figure 6. Multiple Synapses of the Same Axon Innervate Multiple Spines of the Same Postsynaptic Cell

An extreme example in which one axon (blue) innervates five dendritic spines (orange, labeled 1–5) of a basal dendrite (green) is shown. Arrows point to other varicosities of this axon that are innervating dendritic spines of other neurons (data not shown). Scale bar, 2 μm.

synapses (mean 9.9 ± 6.6 μm synapsing versus mean 10.8 ± 5.18 μm touching), providing no support for the idea that innervating axons had a greater affinity to grow along the central dendrite than axons that passed by but did not innervate it (Stepanyants et al., 2004).

We tested whether the axon-spine connectivity observed could be based on purely stochastic mechanisms. Specifically, did redundant excitatory synapses originate by synapse formation among a random subset of the close encounters (i.e., touches) between excitatory axons and dendritic spines? This analysis tests a high-resolution version of the so called Peters' rule (see discussion). We analyzed the 7,505 spine touches and 1,037 synapses between all the excitatory axons (n = 916) with dendritic spines (n = 1,036) in cylinders 1 and 2. For each axon we itemized all the spines that it touched and the subset of these that were actual synapses (Figure 7C). If synaptic connections occurred randomly among the close encounters of axons and spines then a randomization of the synapses among the spine touches should not significantly change the number of times the same axon innervates a dendrite more than once. To assure that each axon in the randomization still established the identical number of synapses as it did in the actual data and that each spine was still innervated by only one excitatory axon (or in 10 cases, two excitatory axons), we developed an algorithm that essentially solved a Sudoku matrix of axons and spines in that it kept the numbers of synapses in the rows and columns unchanged from the actual data (http://openconnecto.me/Kasthurietal2014/Code/touchSynapse; see also the Methods). In this randomization, both the quantitative aspects of the synaptic connectivity of each axon and each dendrite and the spatial overlap of all axons and dendrites are identical to the actual data. The only change made is the particular identity of which of the close axon-spine touches are synaptic. We calculated for each randomization the number of redundant synapses. In a run of 80,000 randomization trials, none of the randomized connectivity patterns had as many redundant synapses as the 78 found in the actual dataset of cylinder 1+2 (simulation median = 52 redundant synapses; $p < 0.00001$; Figure 7D). Thus axon-dendrite adjacency, while of course necessary for synapses to form, is insufficient to explain why some axons establish multiple synapses on some dendrites and not others. This is an explicit refutation of Peters' rule. Rather this result argues that there are different probabilities for synapses between particular dendrites and particular excitatory axons.

To further explore this idea that excitatory axons show preferences in terms of the dendritic spines they innervate (and those they don't) among the larger population of dendritic spines with which they come into close proximity, we carried out an additional test. We analyzed two cohorts of axons from cylinder 1: the 63 axons that innervated the central dendrite's spines within the cylinder (cohort 1) and 63 different excitatory axons that touched the same number of its spines, but did not innervate the central dendrite's spines in the cylinder (cohort 2). Inside the cylinder, the 63 axons in cohort 1 as already described, innervated multiple spines on the central dendrite whereas axons in cohort 2 did not innervate any spines of the central dendrite (by definition) despite both groups having the same access to that dendrite's spines. We then traced these two sets of axons into the surrounding high-resolution volume to see if their synaptic preferences within the cylinder predicted their connectivity preferences outside the cylinder. The results were clear: axons in cohort 1 continued to innervate the central dendrite in the large surrounding volume, adding an additional 11 synapses onto its spines. Axons in cohort 2 however, added only 1 synapse on the central dendrite (Figures 7E and 7F; $p \sim 0.003$; from the binomial distribution, see the Methods). These data show that axons have intrinsic preferences for the spines of some dendrites as opposed to others. However, even among those axons that innervate the central dendrite in the cylinder, some appear better matched to it than others based on their behavior outside the cylinder. Among the axons innervating the central dendrite in the cylinder their likelihood to form additional synapses with it outside the cylindrical volume was in rough proportion to the number of synapses they formed with it in the cylinder. The cohort of axons that established one synapse with the central dendrite in cylinder 1 (n = 52) add 0.13 synapses per axon with it in the larger volume (i.e., excluding the cylinder); those that established two synapses on the central dendrite in the cylinder (n = 8) added 0.38 additional synapses per axon and those axons that established three synapses with the central dendrite in the cylinder (n = 3) added 0.67 additional synapses per axon. Importantly however, these three groups of axons did not differ in their tendency to establish synapses on the sum of all their other dendritic targets indicating that the different synapse biases related to the central dendrite was not accounted for by intrinsically different tendencies to establish synapses among these three cohorts. When all the 63 axons that innervated the central dendrite were considered as a single population ~30% (18/63) of them innervate the central dendrite multiple times. Thus in this region of cortex at least, axons forming multiple synapses

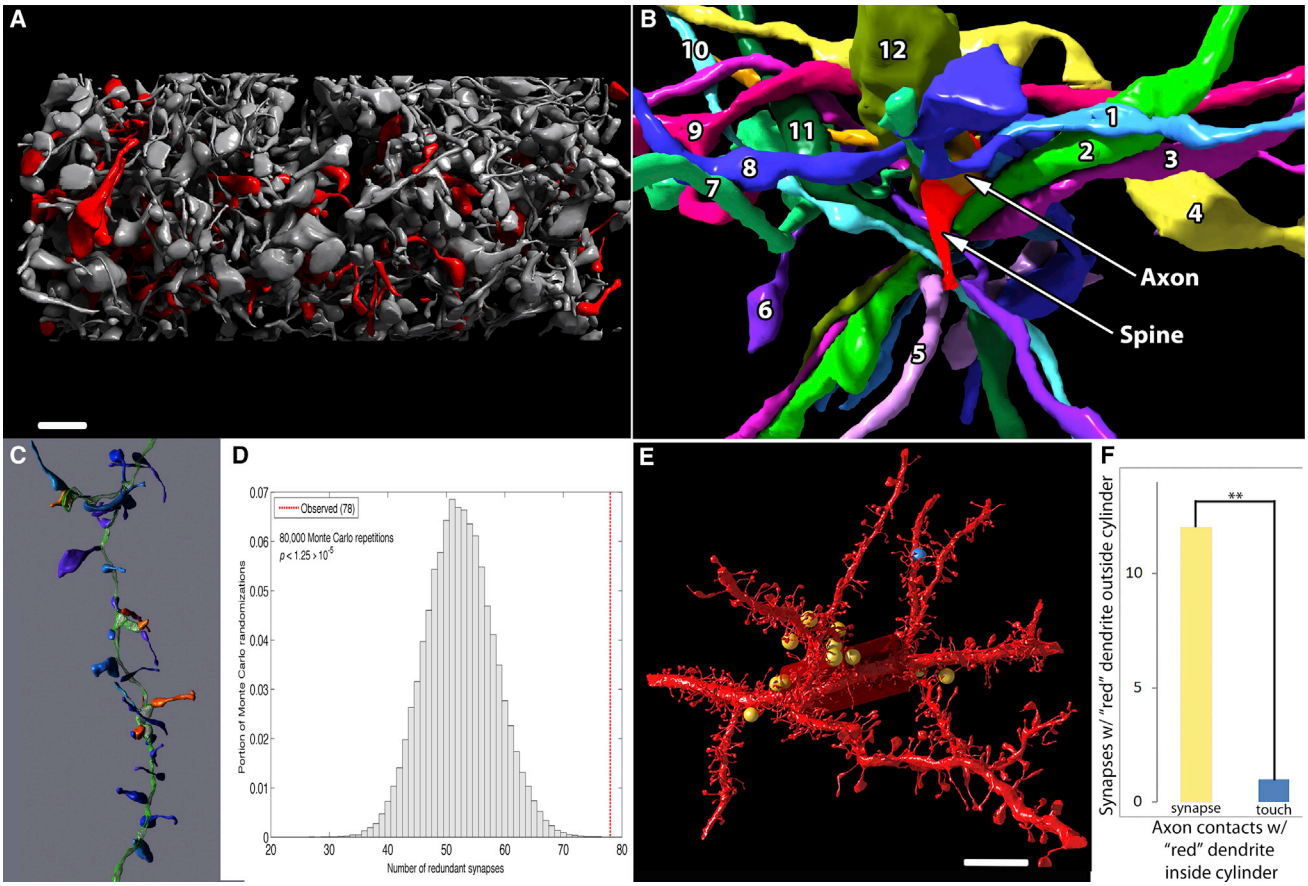

Figure 7. Specificity of Spine Innervation by Excitatory Axons

(A) A rendering demonstrating the high density and intermixing of spines from the red dendrite (red) and many other dendrites (gray) in the cylinder surrounding the "red" apical dendrite. See also Movie S13.

(B) A reconstruction showing 12 additional excitatory axons in the immediate vicinity of a dendritic spine (arrow) and its innervating axon (arrow). See also Movie S14.

(C) A reconstruction showing the nine spines (blue) that "touch" one excitatory axon (green) and the three spines (orange) that are innervated by it.

(D) A histogram showing the number of redundant synapses (see text) in 80,000 randomizations of the synapses among the touches of each axon. In none of these trials was the number of redundant synapses equal to, or greater than, the actual number (red line).

(E) Sites in which the axons that form synapses with the "red" dendrite's spines inside the cylinder establish 11 additional synapses with this dendrite outside the cylinder (yellow spheres). Axons that only touched the "red" dendrite spines in the cylinder form only one synapse with it outside of the cylinder (blue sphere).

(F) A graph showing the result described in (E) ($p = 0.003$). Scale bars, 2 μm for (A) and 15 μm for (E).

See also Figures S5 and S6 and Movies S12, S13, and S14.

on the same dendrite are commonplace and the tendency appears to be graded: some axons consistently avoid synapses with some dendrites, and among those that do form synapses with a dendrite, there appear to be a range of tendencies from weak to strong.

Synapses with Identical Activity

The high incidence of multiple synapses of one axon on one dendrite offers an opportunity to study spine synapses with nearly identical pre- and postsynaptic activity patterns. Are structural properties of synapses regulated by activity patterns? Such tests have been carried out in the hippocampus suggesting that they do (Sorra et al., 1998) and here we examine if the trends are the same in neocortex. We use the synapse dataset (Table S1) to compare five structural features of pairs of synapses established by the same axon on pairs of dendritic spines of the same dendrite. To assess whether synapses of the same axon on the same dendrite show more similarity than would be expected if synapse structures at each site are independently and randomly determined, we compared the measured values between the actual pairs with randomly chosen pairs from the same cohort by doing a permutation test.

The overall conclusion we reach is that pairs of excitatory synapses that have identical pre- and postsynaptic partners tend to be more similar than randomly chosen pairs from the same cohort for 4 of the 5 metrics (mitochondria in the synaptic terminal being the exception) but that for our data sample, this only reaches statistical significance for measures of the volume of dendritic spines. The evidence for similarity is stronger at pairs

sharing both the same axon and the same dendrite than pairs sharing either just the same axon (on different dendrites) or just the same dendrite (but from different axons).

DISCUSSION

The aim of this work was to turn EM images of brain into a minable dataset for multiple analyses without the need for new image data for each question (Figure S7). The vast majority of our effort occurred after generating the segmented images as we learned how to transform images into a database and analyze it. The synapse database (Table S1) provides such a resource for the connections within the volume as demonstrated by some of the queries and results in this paper.

In the last few years there have been a number of detailed analyses of neural ultrastructure and its relation to functional properties of neurons. In this paper we depart from this approach in that there were no antecedent functional studies to focus our analysis. The goal rather was to see what could be learned from a saturated connectomic analysis per se in neocortex. Part of the motivation was to explicitly consider the fact that connectomics can reveal structure where functional information is not available in analogy to the way genomics reveals sequences of genes whose function are not yet known. To allow for further inquiries and analyses in the high-resolution volume (80,000 μm^3) we provide access to all the image data via the Open Connectome Project (http://openconnecto.me/Kasthurietal2014/), the 2D and 3D visualization, tracing, and editing tools, many of which were developed specifically for this project. Moreover, much of the analytic software developed for this project is also available (http://openconnecto.me/Kasthurietal2014/Code).

We analyzed the synapses of excitatory axons with dendritic spines, the most plentiful synapses in the saturated volume to learn if their connectivity could be predicted by simply knowing the degree of physical overlap of axons and dendrites. This idea underpins theoretical approaches to understanding the brain (Braitenberg and Schuz, 1998; da Costa and Martin, 2013). Explaining synaptic connectivity by physical overlap is an attractive idea because of the obviously laminated organization of many regions of the brain including the cerebral cortex. Evidence supports the idea that molecular cues guide innervating terminal axon branches and perhaps postsynaptic dendrites to particular regions where they can form synapses with each other (Williams et al., 2010). It is thus possible that synaptic specificity in the cortex is explained in large part by axon and dendrite guidance mechanisms that put pre- and postsynaptic elements in close proximity (i.e., the same layer or sub-layer). If so, this would simplify the analysis of cortical connectivity and support models based largely on areal projections of axons and the classes of dendrites in their terminal fields. Such statistical approaches potentially provide a way to model brains without requiring knowing the exact details of every neuron's connections (Binzegger et al., 2004; Hill et al., 2012). This concept, called Peters' Rule, after Alan Peters (despite his insistence that he disputes it—A. Peters, personal communication) has been examined in retina and hippocampus. In retina some data support the idea that, to at least some degree, the contacts (probably synapses) between neurons can be accounted for by their proximity, in support of Peters' Rule (Kim et al., 2014). However even that work found the numbers of contacts were skewed from what one would expect if proximity were the only factor guiding contacts. In a different piece of work from the same serial dataset the directional selectivity of individual amacrine dendrites looked to be arranged in a way that was incompatible with random contacts (Briggman et al., 2011). In hippocampus, support for the idea that connectivity was not explicable simply by proximity has also been obtained (Mishchenko et al., 2010; Druckmann et al., 2014). The previous results do not explicitly test the degree to which actual proximity of each individual axon to all the postsynaptic sites in a volume explains the connectivity patterns observed.

We therefore used the saturated reconstruction to identify each place each excitatory axon comes within touching distance to a dendritic spine. We discovered that each spine is closely apposed by about nine different axons (of which typically only one establishes a synapse). This means that one must use some caution in light microscopy when claiming an axon and a nearby dendritic spine are making synaptic contact. Our results argue for the idea that cellular identity, and not proximity, guides the connections between excitatory axons and dendritic spines. The best predictor of whether an axon would establish a synapse with a particular dendrite was its synaptic connectivity with that dendrite at other sites. An excitatory axon that established a spine synapse with a dendrite, had a 40% probability of establishing another synapse on the same dendrite whereas excitatory axons that only came adjacent to, but did not innervate, a dendrite's spine had a 25-fold lower probability (~1.6%) of establishing a synapse with that dendrite at another site. Thus while physical overlap of axons and dendrites is necessary, it is not sufficient to generate the pattern of synaptic connections in this region of cerebral cortex, refuting Peters' rule.

The abundance of multiple spine synapses of the same excitatory axon on the same dendrite suggests that the strength of excitatory connections here, as elsewhere in the brain, is based on the number of synapses between them and can range from zero to a potentially large number. Changes in the number of spine synapses between an axon and a dendrite could be downstream of short term alterations in synaptic efficacy (such as by changes in neurotransmitter receptor number or spine shape at individual synapses). In distinction to synaptic efficacy, such numerical changes in connectivity may be longer lasting and may be less reversible. Indeed, developmental synapse elimination in the peripheral nervous system occurs in this way: changes in efficacy are followed by addition of new synaptic sites (Colman et al., 1997). If comparable developmental processes of synapse elimination and compensatory synapse addition that are known to occur in the peripheral nervous system, and some parts of the CNS (Hashimoto and Kano, 2005; Walsh and Lichtman, 2003), are also occurring in the cerebral cortex, then the pattern of connectivity seen here might occur as a consequence of similar activity-dependent mechanisms. In particular, if synapse elimination removes some of the axonal input converging on a pyramidal cell, then remaining inputs might locally sprout to occupy vacated spines in much the same way remaining motor axons takeover sites vacated by eliminated axons at

the developing neuromuscular junction (Walsh and Lichtman, 2003; Turney and Lichtman, 2012). Saturated reconstructions of neural circuits in younger cerebral cortex may therefore be informative.

Finally, given the many challenges we encountered and those that remain in doing saturated connectomics, we think it is fair to question whether the results justify the effort expended. What after all have we gained from all this high density reconstruction of such a small volume? In our view, aside from the realization that connectivity is not going to be easy to explain by looking at overlap of axons and dendrites (a central premise of the Human Brain Project (Markram et al., 2012), we think that this "omics" effort lays bare the magnitude of the problem confronting neuroscientists who seek to understand the brain. Although technologies, such as the ones described in this paper, seek to provide a more complete description of the complexity of a system, they do not necessarily make understanding the system any easier. Rather, this work challenges the notion that the only thing that stands in the way of fundamental mechanistic insights is lack of data. The numbers of different neurons interacting within each miniscule portion of the cortex is greater than the total number of different neurons in many behaving animals. Some may therefore read this work as a cautionary tale that the task is impossible. Our view is more sanguine; in the nascent field of connectomics there is no reason to stop doing it until the results are boring.

EXPERIMENTAL PROCEDURES

A detailed description is available in the Supplemental Experimental Procedures.

Data Acquisition

An anesthetized adult mouse was perfused transcardially with a fixative solution containing glutaraldehyde, paraformaldehyde, and $CaCl_2$ in cacodylate buffer. The brain was removed and maintained overnight at 4°C in the same fixative solution. A 200-μm vibratome section encompassing part of the somatosensory cortex was then removed, washed, and stained with reduced osmium tetroxide-thiocarbohydrazide (TCH)-osmium ("ROTO") and infiltrated with Epon (for details, see Tapia et al., 2012). The cured block was trimmed to a 2 × 3 mm rectangle and a depth of 200 μm and then readied for automated serial sectioning. The automated, unattended collection of 29.4-nm serial sections was accomplished using a custom tape collection device attached to a commercial ultramicrotome (ATUM). The sections were collected on plasma-treated polyamide (Kapton, Sheldahl) 8-mm-wide tape. The tape was then cut into strips and attached to silicon wafers (Figure 1). The wafers with sections were then coated with ~10 nm of carbon to ensure conductivity. An automated protocol to locate and image sections on the wafers was used (Hayworth et al., 2014; see also Tomassy et al., 2014) with a Sigma scanning electron microscope (Carl Zeiss), equipped with the ATLAS software (Fibics). The serial section images were acquired using backscattered electron detection. Single images using secondary electron detection were acquired using the FEI Magellan thru-the-lens detector or the Zeiss MultiSEM 505. Sections collected on carbon-coated Kapton were required for secondary electron detection.

For the medium- and high-resolution data sets, alignment was accomplished by affine image transformations using custom Matlab scripts. The high-resolution image stack (1,850 images) was aligned using a single affine transformation per image. The aligned images were then manually segmented using a custom Direct3D-based Windows volume annotation and segmentation tool (VAST; http://openconnecto.me/Kasthurietal2014/Code/VAST). The segmented images and metadata were processed for data analysis with Matlab scripts and 3D rendering with Matlab scripts for computation of surface meshes and 3 dsMax (Autodesk) for the rendering steps. We also developed RhoANA, a processing pipeline, to generate automatic segmentations, and Mojo, a proofreading tool. All code is open source and available online at http://www.rhoana.org/. In order to scale to large data sets, we designed the processing pipeline to run on a computer cluster.

Data Analysis

Excitatory (E) and inhibitory (I) synapses were classified according to established criteria (Peters et al., 1991). If a particular synapse was ambiguous, additional synapses of the same axon were found and analyzed until a clear assignment could be made. In any section synaptic vesicles were only counted that showed a clear center, and this is an accurate measure of the total number of vesicles (Figure S4). We utilized the Open Connectome Project, which has developed the Reusable Annotation Markup for Open coNnectomics (RAMON), a spatial database to store large-scale images and co-registered annotation datasets (Burns et al., 2013). To assess whether the observed number of "redundant" synapses (defined as the number of synapses in excess of one that an axon and dendrite "share"), we used Monte Carlo reassignment of the synapses (the Sudoku algorithm) among all the close contacts each axon established with dendritic spines described in detail in the Supplemental Experimental Procedures. To estimate the number of objects within the cylinder that are likely to be branches of the same axon, we used a set of cortical axon skeletons available at the NeuroMorpho web site (Ascoli et al., 2007) and a Monte Carlo simulation in which the cylinder is randomly translated so that at least one branch overlaps, and we count the number of times a second branch is also in the cylinder. To assess the similarity of pairs of synapses made by the same axon on the same dendrite, we select all the pairs of synapses shared by the same axon and same dendrite (SASD) from the spreadsheet in Table S1 and use the values of five morphological metrics for statistical analysis.

SUPPLEMENTAL INFORMATION

Supplemental Information includes Supplemental Experimental Procedures, 7 figures, 1 table, and 14 movies and can be found with this article online at http://dx.doi.org/10.1016/j.cell.2015.06.054.

AUTHOR CONTRIBUTIONS

ATUM, N.K., K.J.H., R.L.S., N.K. J.C.T., and J.W.L.; sample preparation, N.K., R.L.S., J.C.T., and J.W.L.; optimization of scanning electron microscope and imaging (tape substrates, wafer creation, etc.), N.K., R.L.S., J.C.T., and J.W.L.; semi-automatic acquisition of data, N.K., D.R.B., R.L.S., and J.W.L., alignment, D.R.B.; VAST, D.R.B., and H.S.S.; manual segmentation*, N.K., D.R.B., and D.L.; automatic segmentation pipeline (RhoANA, Mojo, etc.), S.K.B., A.V.R., V.K., T.R.J., M.R., H.P., and J.W.L. statistical analyses, N.K., D.R.B., J.A.C., T.R.J., J.L.M., W.G.R., J.T.V., D.L.S., C.E.P., and J.W.L.; 3D renderings, D.R.B. and N.K.; online database management (openconnectome, etc.), W.G.R., J.T.V., and R.B.; writing, N.K., D.R.B., R.L.S., J.C.T., H.S.S., and J.W.L.

ACKNOWLEDGMENTS

We gratefully acknowledged support from the NIH/NINDS (1DP2OD006514-01, TR01 1R01NS076467-01, and 1U01NS090449-01), Conte (1P50MH094271-01), MURI Army Research Office (contract no. W911NF1210594 and IIS-1447786), CRCNS 1R01EB016411), NSF (OIA-1125087 and IIS-1110955), DARPA (HR0011-14-2-0004), the Human Frontier Science Program (RGP0051/2014), the JHU Applied Physics Laboratory, the Research Program for Applied Neuroscience, the Howard Hughes Medical Institute, Nvidia, Intel, and Google. We are also grateful to the Center for the Developing Child at Harvard University for providing tracers, Masconomet Regional High School, and Priya Manavalan and Kunal Lillaney at the Open Connectome Project for help with data management.

Received: October 19, 2014
Revised: March 10, 2015
Accepted: June 1, 2015
Published: July 30, 2015

REFERENCES

Anderson, J.R., Jones, B.W., Watt, C.B., Shaw, M.V., Yang, J.H., Demill, D., Lauritzen, J.S., Lin, Y., Rapp, K.D., Mastronarde, D., et al. (2011). Exploring the retinal connectome. Mol. Vis. *17*, 355–379.

Araya, R., Jiang, J., Eisenthal, K.B., and Yuste, R. (2006). The spine neck filters membrane potentials. Proc. Natl. Acad. Sci. USA *103*, 17961–17966.

Ascoli, G.A., Donohue, D.E., and Halavi, M. (2007). NeuroMorpho.Org: a central resource for neuronal morphologies. J. Neurosci. *27*, 9247–9251.

Beierlein, M., Gibson, J.R., and Connors, B.W. (2003). Two dynamically distinct inhibitory networks in layer 4 of the neocortex. J. Neurophysiol. *90*, 2987–3000.

Benavides-Piccione, R., Ballesteros-Yáñez, I., DeFelipe, J., and Yuste, R. (2002). Cortical area and species differences in dendritic spine morphology. J. Neurocytol. *31*, 337–346.

Binzegger, T., Douglas, R.J., and Martin, K.A. (2004). A quantitative map of the circuit of cat primary visual cortex. J. Neurosci. *24*, 8441–8453.

Bock, D.D., Lee, W.C., Kerlin, A.M., Andermann, M.L., Hood, G., Wetzel, A.W., Yurgenson, S., Soucy, E.R., Kim, H.S., and Reid, R.C. (2011). Network anatomy and in vivo physiology of visual cortical neurons. Nature *471*, 177–182.

Braitenberg, V., and Schuz, A. (1998). Cortex: Statistics and Geometry of Neuronal Connectivity (Berlin: Springer).

Briggman, K.L., Helmstaedter, M., and Denk, W. (2011). Wiring specificity in the direction-selectivity circuit of the retina. Nature *471*, 183–188.

Burns, R., Roncal, W.G., Kleissas, D., Lillaney, K., Manavalan, P., Perlman, E., Berger, D.R., Bock, D.D., Chung, K., Grosenick, L., et al. (2013). The open connectome project data cluster: Scalable analysis and vision for high-throughput neuroscience. A. Szalay, T. Budavari, M. Balazinska, A. Meliou, and A. Sacan, eds. Proceedings of the 25th International Conference on Scientific and Statistical Database Management.

Cajal, R.S. (1899). Textura del sistema nervioso del hombre y de los vertebrados (Madrid: Moya).

Chicurel, M.E., and Harris, K.M. (1992). Three-dimensional analysis of the structure and composition of CA3 branched dendritic spines and their synaptic relationships with mossy fiber boutons in the rat hippocampus. J. Comp. Neurol. *325*, 169–182.

Colman, H., Nabekura, J., and Lichtman, J.W. (1997). Alterations in synaptic strength preceding axon withdrawal. Science *275*, 356–361.

da Costa, N.M., and Martin, K.A. (2013). Sparse reconstruction of brain circuits: or, how to survive without a microscopic connectome. Neuroimage *80*, 27–36.

Deans, J.K., Powell, A.D., and Jefferys, J.G. (2007). Sensitivity of coherent oscillations in rat hippocampus to AC electric fields. J. Physiol. *583*, 555–565.

DeFelipe, J., and Fariñas, I. (1992). The pyramidal neuron of the cerebral cortex: morphological and chemical characteristics of the synaptic inputs. Prog. Neurobiol. *39*, 563–607.

Druckmann, S., Feng, L., Lee, B., Yook, C., Zhao, T., Magee, J.C., and Kim, J. (2014). Structured synaptic connectivity between hippocampal regions. Neuron *81*, 629–640.

Eberle, A.L., Mikula, S., Schalek, R., Lichtman, J.W., Tate, M.L., and Zeidler, D. (2015). High-resolution, high-throughput imaging with a multibeam scanning electron microscope. J. Microsc. Published online January 27, 2015. http://dx.doi.org/10.1111/jmi.12224.

Friedman, P.L., and Ellisman, M.H. (1981). Enhanced visualization of peripheral nerve and sensory receptors in the scanning electron microscope using cryofracture and osmium-thiocarbohydrazide-osmium impregnation. J. Neurocytol. *10*, 111–131.

Gulyás, A.I., Megías, M., Emri, Z., and Freund, T.F. (1999). Total number and ratio of excitatory and inhibitory synapses converging onto single interneurons of different types in the CA1 area of the rat hippocampus. J. Neurosci. *19*, 10082–10097.

Haehn, D., Knowles-Barley, S., Roberts, M., Beyer, J., Kasthuri, N., Lichtman, J.W., and Pfister, H. (2014). Design and evaluation of interactive proofreading tools for connectomics. Proceedings of IEEE Transactions on Visualization and Computer Graphics.

Hashimoto, K., and Kano, M. (2005). Postnatal development and synapse elimination of climbing fiber to Purkinje cell projection in the cerebellum. Neurosci. Res. *53*, 221–228.

Hayworth, K.J., Morgan, J.L., Schalek, R., Berger, D.R., Hildebrand, D.G., and Lichtman, J.W. (2014). Imaging ATUM ultrathin section libraries with WaferMapper: a multi-scale approach to EM reconstruction of neural circuits. Front. Neural Circuits *8*, 68.

Helmstaedter, M., Briggman, K.L., and Denk, W. (2011). High-accuracy neurite reconstruction for high-throughput neuroanatomy. Nat. Neurosci. *14*, 1081–1088.

Helmstaedter, M., Briggman, K.L., Turaga, S.C., Jain, V., Seung, H.S., and Denk, W. (2013). Connectomic reconstruction of the inner plexiform layer in the mouse retina. Nature *500*, 168–174.

Hill, S.L., Wang, Y., Riachi, I., Schürmann, F., and Markram, H. (2012). Statistical connectivity provides a sufficient foundation for specific functional connectivity in neocortical neural microcircuits. Proc. Natl. Acad. Sci. USA *109*, E2885–E2894.

Kaynig, V., Vazquez-Reina, A., Knowles-Barley, S., Roberts, M., Jones, T.R., Kasthuri, N., Miller, E., Lichtman, J.W., and Pfister, H. (2013). Large scale automatic reconstruction of neuronal processes from electron microscopy images. arXiv, arXiv:1303.7186, http://arxiv.org/abs/1303.7186.

Kim, J.S., Greene, M.J., Zlateski, A., Lee, K., Richardson, M., Turaga, S.C., Purcaro, M., Balkam, M., Robinson, A., Behabadi, B.F., et al.; EyeWirers (2014). Space-time wiring specificity supports direction selectivity in the retina. Nature *509*, 331–336.

Krieger, P., Kuner, T., and Sakmann, B. (2007). Synaptic connections between layer 5B pyramidal neurons in mouse somatosensory cortex are independent of apical dendrite bundling. J. Neurosci. *27*, 11473–11482.

Li, Z., Okamoto, K., Hayashi, Y., and Sheng, M. (2004). The importance of dendritic mitochondria in the morphogenesis and plasticity of spines and synapses. Cell *119*, 873–887.

Lichtman, J.W., Pfister, H., and Shavit, N. (2014). The big data challenges of connectomics. Nat. Neurosci. *17*, 1448–1454. http://dx.doi.org/10.1038/nn.3837.

Marblestone, A., Daugharthy, E., Kalhor, R., Peikon, I., Kebschull, J., Shipman, S., Mishchenko, Y., Dalrymple, D., Zamft, B., Kording, K., Boyden, E., Zador, A., and Church, G. (2013). Conneconomics: The economics of large-scale neural connectomics. http://dx.doi.org/10.1101/001214.

Markram, H., Lubke, J., Frotscher, M., Roth, A., and Sakmann, B. (1997). Physiology and anatomy of synaptic connections between thick tufted pyramidal neurones in the developing rat neocortex. J. Physiol. *500* (Pt 2), 409–440.

Markram, H., Wang, Y., and Tsodyks, M. (1998). Differential signaling via the same axon of neocortical pyramidal neurons. Proc. Natl. Acad. Sci. USA *95*, 5323–5328.

Markram, H., Ailamaki A., Alvandpour A., Amunts K., Andreoni W., Ashburner J., Axer M., Baaden M., Badia R., Bartolome J., et al. (2012). The human brain project: A report to the European Commission. https://www.humanbrainproject.eu/documents/10180/17648/TheHBPReport_LR.pdf/18e5747e-10af-4bec-9806-d03aead57655.

Megías, M., Emri, Z., Freund, T.F., and Gulyás, A.I. (2001). Total number and distribution of inhibitory and excitatory synapses on hippocampal CA1 pyramidal cells. Neuroscience *102*, 527–540.

Mishchenko, Y. (2009). Automation of 3D reconstruction of neural tissue from large volume of conventional serial section transmission electron micrographs. J. Neurosci. Methods *176*, 276–289.

Mishchenko, Y., Hu, T., Spacek, J., Mendenhall, J., Harris, K.M., and Chklovskii, D.B. (2010). Ultrastructural analysis of hippocampal neuropil from the connectomics perspective. Neuron *67*, 1009–1020.

Mountcastle, V.B. (1997). The columnar organization of the neocortex. Brain *120*, 701–722.

Nunez-Iglesias, J., Kennedy, R., Plaza, S.M., Chakraborty, A., and Katz, W.T. (2014). Graph-based active learning of agglomeration (GALA): a Python library to segment 2D and 3D neuroimages. Front. Neuroinform. *8*, 34.

Peters, A., Josephson, K., and Vincent, S.L. (1991). Effects of aging on the neuroglial cells and pericytes within area 17 of the rhesus monkey cerebral cortex. Anat. Rec. *229*, 384–398.

Plaza, S.M., Scheffer, L.K., and Chklovskii, D.B. (2014). Toward large-scale connectome reconstructions. Curr. Opin. Neurobiol. *25*, 201–210.

Popov, V.I., and Stewart, M.G. (2009). Complexity of contacts between synaptic boutons and dendritic spines in adult rat hippocampus: three-dimensional reconstructions from serial ultrathin sections in vivo. Synapse *63*, 369–377.

Purpura, D.P. (1975). Dendritic differentiation in human cerebral cortex: normal and aberrant developmental patterns. Adv. Neurol. *12*, 91–134.

Sherrington, C. (1906). The Integrative Action of the Nervous System (Yale: Yale University Press).

Sinha, A., Roncal, W.G., Kasthuri, N., Lichtman, J.W., Burns, R., and Kazhdan, M. (2013). Automatic annotation of axoplasmic reticula in pursuit of connectomes using high resolution neural EM data. 3rd Annual Hopkins Imaging Conference.

Smiley, J.F., and Goldman-Rakic, P.S. (1993). Heterogeneous targets of dopamine synapses in monkey prefrontal cortex demonstrated by serial section electron microscopy: a laminar analysis using the silver-enhanced diaminobenzidine sulfide (SEDS) immunolabeling technique. Cereb. Cortex *3*, 223–238.

Song, S., Sjöström, P.J., Reigl, M., Nelson, S., and Chklovskii, D.B. (2005). Highly nonrandom features of synaptic connectivity in local cortical circuits. PLoS Biol. *3*, e68.

Sorra, K.E., Fiala, J.C., and Harris, K.M. (1998). Critical assessment of the involvement of perforations, spinules, and spine branching in hippocampal synapse formation. J. Comp. Neurol. *398*, 225–240.

Stepanyants, A., and Chklovskii, D.B. (2005). Neurogeometry and potential synaptic connectivity. Trends Neurosci. *28*, 387–394.

Stepanyants, A., Tamás, G., and Chklovskii, D.B. (2004). Class-specific features of neuronal wiring. Neuron *43*, 251–259.

Takemura, S.Y., Bharioke, A., Lu, Z., Nern, A., Vitaladevuni, S., Rivlin, P.K., Katz, W.T., Olbris, D.J., Plaza, S.M., Winston, P., et al. (2013). A visual motion detection circuit suggested by Drosophila connectomics. Nature *500*, 175–181.

Tapia, J.C., Kasthuri, N., Hayworth, K.J., Schalek, R., Lichtman, J.W., Smith, S.J., and Buchanan, J. (2012). High-contrast en bloc staining of neuronal tissue for field emission scanning electron microscopy. Nat. Protoc. *7*, 193–206.

Tomassy, G.S., Berger, D.R., Chen, H.H., Kasthuri, N., Hayworth, K.J., Vercelli, A., Seung, H.S., Lichtman, J.W., and Arlotta, P. (2014). Distinct profiles of myelin distribution along single axons of pyramidal neurons in the neocortex. Science *344*, 319–324.

Turney, S.G., and Lichtman, J.W. (2012). Reversing the outcome of synapse elimination at developing neuromuscular junctions in vivo: evidence for synaptic competition and its mechanism. PLoS Biol. *10*, e1001352.

van Vreeswijk, C., and Sompolinsky, H. (1996). Chaos in neuronal networks with balanced excitatory and inhibitory activity. Science *274*, 1724–1726.

Vanharreveld, A., Crowell, J., and Malhotra, S.K. (1965). A study of extracellular space in central nervous tissue by freeze-substitution. J. Cell Biol. *25*, 117–137.

Vazquez-Reina, A., Gelbart, M., Huang, D., Lichtman, J., Miller, E.L., Pfister, H. (2011). Segmentation fusion for connectomics. Proceedings of IEEE International Conference on Computer Vision, 177–184.

Walsh, M.K., and Lichtman, J.W. (2003). In vivo time-lapse imaging of synaptic takeover associated with naturally occurring synapse elimination. Neuron *37*, 67–73.

Wehr, M., and Zador, A.M. (2003). Balanced inhibition underlies tuning and sharpens spike timing in auditory cortex. Nature *426*, 442–446.

White, J.G., Southgate, E., Thomson, J.N., and Brenner, S. (1986). The structure of the nervous system of the nematode Caenorhabditis elegans. Philos. Trans. R. Soc. Lond. B Biol. Sci. *314*, 1–340.

Williams, M.E., de Wit, J., and Ghosh, A. (2010). Molecular mechanisms of synaptic specificity in developing neural circuits. Neuron *68*, 9–18.

Cell

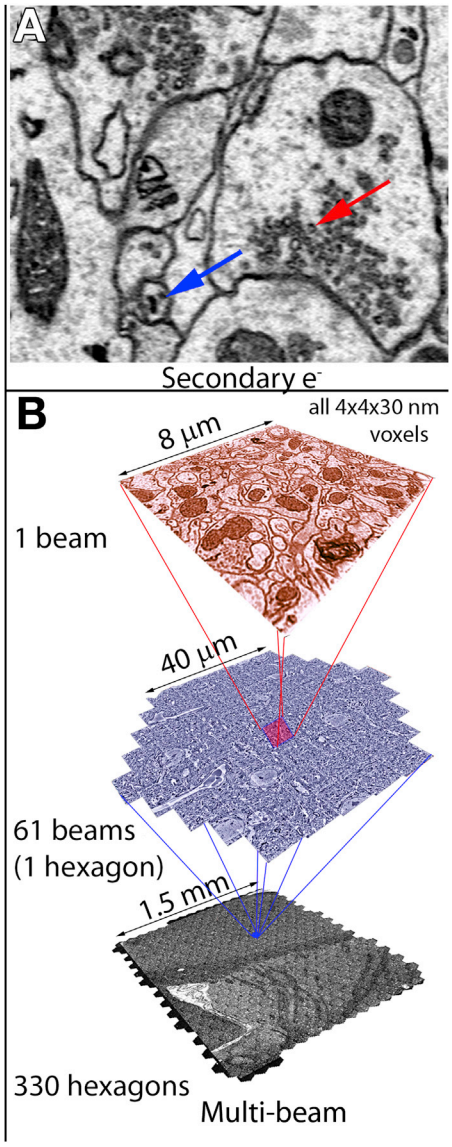

Figure S1. Imaging a Brain on Tape with Secondary Electrons, Related to Figure 2

(A) A 29 nm section of neocortex imaged by detecting secondary electrons using a 1.7 keV beam in a scanning electron microscope. This approach also has sufficient resolution to detect synaptic vesicles (red arrow) and the endoplasmic reticulum (blue arrow).

(B) To speed image acquisition, multiple electron beams scanning in parallel have been developed in a new scanning electron microscope. This device has 61 scanning beams and detects secondary electrons with the potential of speeding up acquisition from millions to billions of pixels per second. Shown is an image of mouse cortex (red, top) generated by a single beam which is part of a 61 beam hexagonal array of simultaneously acquired images (blue, middle). These hexagons can be tiled by stage movement to generate a large field of view (bottom).

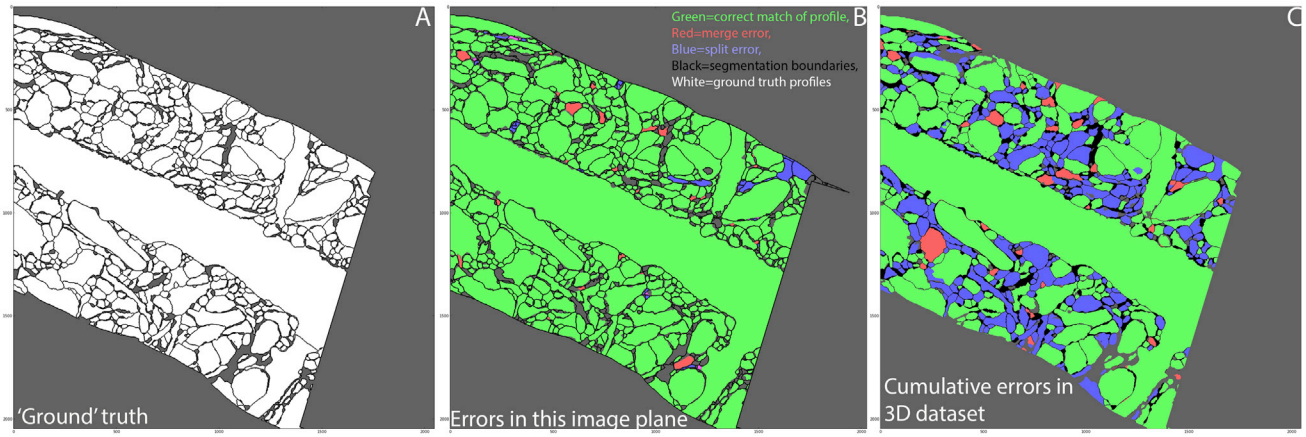

Figure S2. 2D and 3D Errors from Automatic Segmentation Output of RhoANA with GALA, Related to Figure 3

(A) Ground truth segmentation of the boundaries of cellular objects in a single slice.

(B) Error analysis of automatic segmentation output for the same EM slice. Cellular profiles that are incorrectly segmented in this single image are identified as merge or spilt errors.

(C) Error analysis of automatic segmentation output for the same EM slice as (A) and (B) but now objects that have an error anywhere in the 3D stack are identified. Output is color coded as follows: Green = correct match, Red = merge error, Blue = split error, Black = segmentation boundaries, and White = ground truth profiles (ground truth image only). The output of the automatic segmentation is classified as a correct match if there is reciprocal-majority overlap with the segmentation output and the 'ground' truth annotations. Profile errors smaller than 0.0011um^3 and 3D errors smaller than 0.0054 μm^3 are not shown.

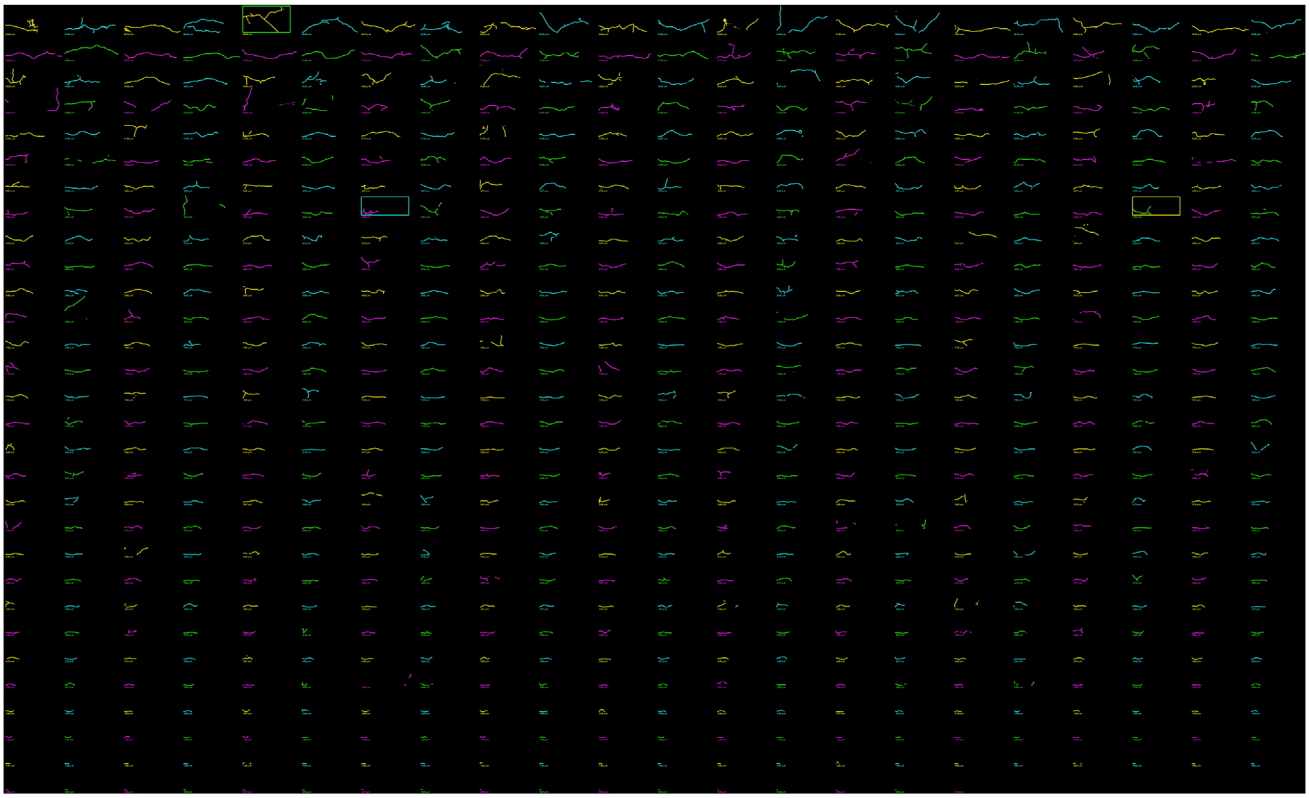

Figure S3. A List of All the Excitatory Axons in Cylinder 1 of the Saturated Reconstruction, Related to Figure 3

Shown are skeletonizations of all 660 excitatory axons ordered from longest (top left) to shortest lengths (bottom right). Total length of each axon within the cylinder in μms is indicated below each axon. Only 3 axons (boxes) have non-terminal branches.

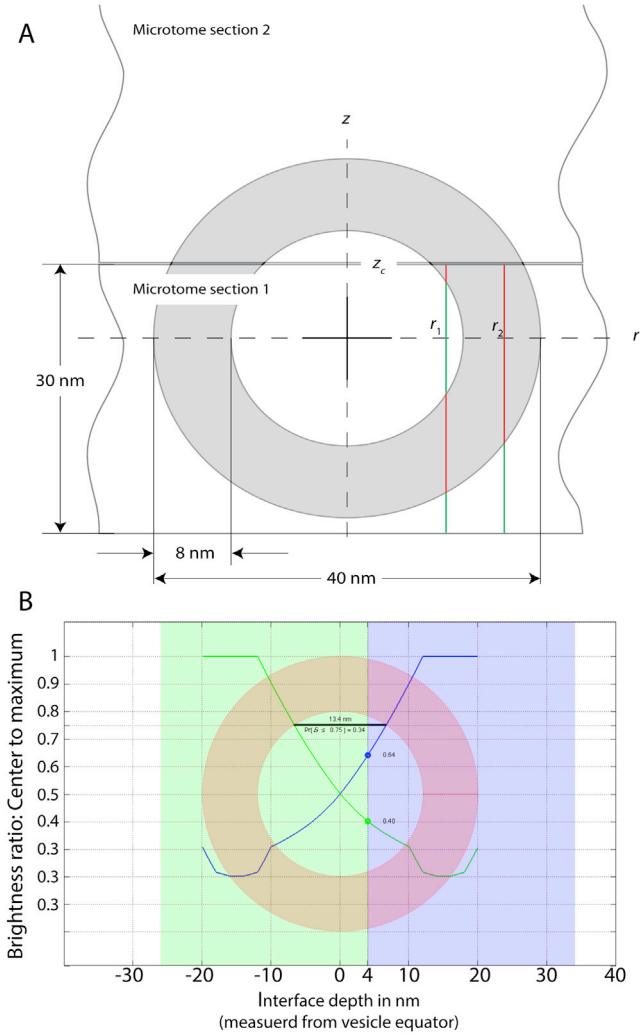

Figure S4. Calculating the Number of Synaptic Vesicles in Electron Microscopy Ultrathin Serial Sections, Related to Figure 5

(A) A Matlab script goes over a grid of lateral distances away from the vesicle center in one axis (*r*-axis) and distance from the vesicle center at which the portion of the vesicle within the section begins (z_c). At each radius *r* (e.g., r_1 and r_2 in the figure) we calculate the thickness for each depth z_c from a vertical line through the section (shown for section 1). The thickness is the length of the red portions of the vertical lines at r_1 and r_2. A similar calculation is done for the adjacent serial section (2).

(B) The horizontal axis is the distance from the vesicle's center at which the two sections (green and violet rectangles) split the vesicle. The vertical axis is the ratio of the brightness at the center to the maximum brightness in the vesicle's image. The figure shows two brightness profiles. The green one is for the light-green section on the left-hand-side of the figure, the blue one for the adjacent section (violet rectangle at the right). The figure shows also an example of how to read the graph for the case when the vesicle is split at 4 nm above its center. Following a vertical line from the 4 nm mark we read from the green profile the relative brightness at vesicle center in the green section (0.40) and from the blue profile the relative gray level in the violet section (0.64). The two profiles cross at a relative brightness of 0.5. That is, when the brightness at the center is 50% of the brightest portion of the vesicle image. Consequently, it is not possible for both sections to show, for the same vesicle, a core brighter than 50% its membrane intensity. Thus counting the number of vesicles with bright centers in a serial stack of images provides the number of synaptic vesicles.

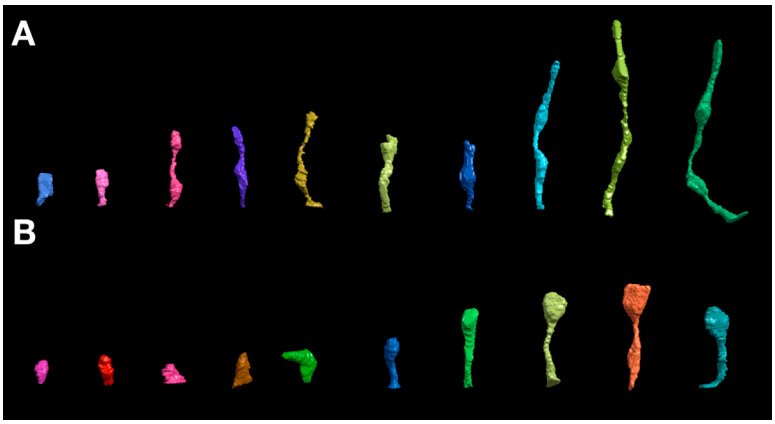

Figure S5. Morphology of Spines and Filopodia, Related to Figure 7

(A and B) Shown are three dimensional renderings of 10 size matched filopodia that lack presynaptic partners (A) and 10 innervated dendritic spines (B) ordered from left to right in increasing size.

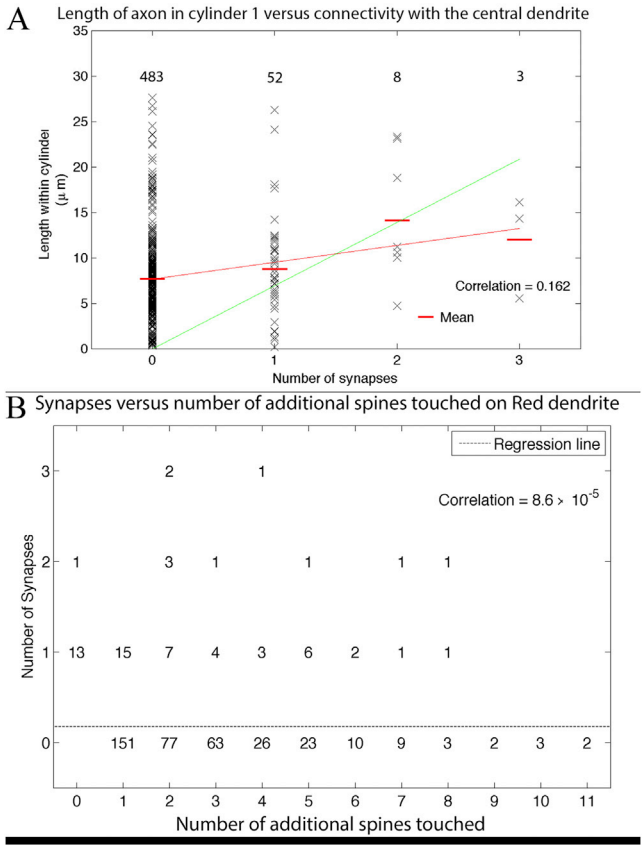

Figure S6. Axonal Proximity to Either a Dendrite or Its Spines Is Not a Strong Predictor of Synaptic Connectivity, Related to Figure 7

(A) Graph that shows that the average length of axons (represented by discrete red lines) was weakly correlated with the number of synapses established by those axons on the central dendrite in cylinder 1 (Red line; R = 0.162, assuming normally-distributed, homoschedastic residuals). Shown are the lengths of all the axons that intersected the cylinder arranged by the number of synapses they established on the central dendrite (which received the largest share of synapses of any dendrite in the cylinder). This data does not provide strong support for the idea that it is simply the amount of axonal overlap with the cylindrical spinous territory surrounding an apical dendrite that explains the degree of synaptic coupling (the green line is a least-squares fit of a line that would indicate that the number of synapses is proportional to the axon's length in the neighborhood of the dendrite. If two quantities in a plot are proportional to each other, the line passes through the origin).

(B) Graph compares the number of synapses axons established with the number of times an axon came within the immediate proximity of a spine without forming a synapse. If the probability of synapse formation between an axon and a dendrite was proportional to the number of times that axon was immediately adjacent to the spines of that dendrite, then the axons that innervated the central dendrite the most times should have had more opportunities as evidenced by more close encounters (touches). The data do not support this idea and instead show a weak correlation r = 0.000086 between the number of synapse formed and the number of spines touched (dotted line is the horizontal least-squares regression line).

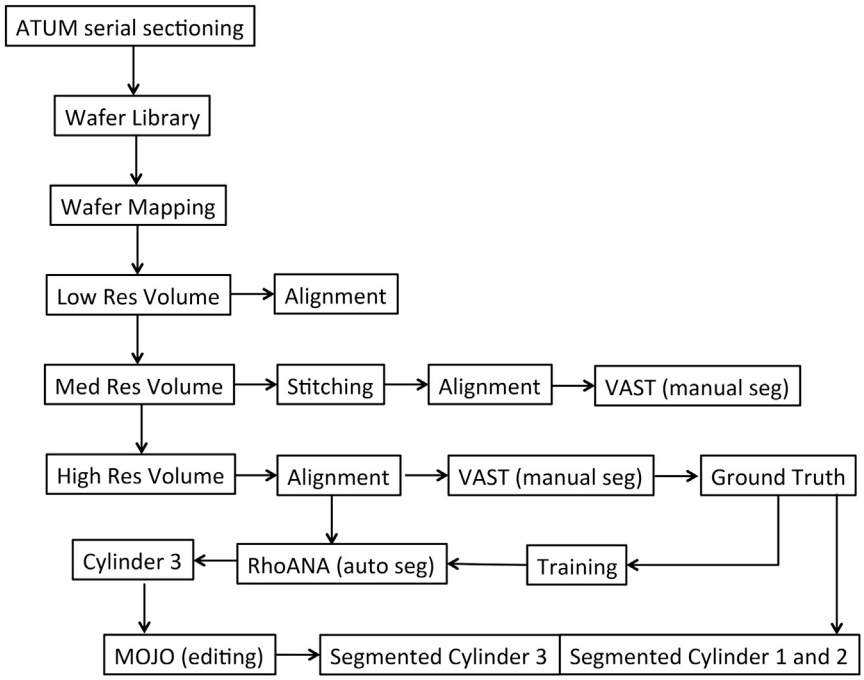

Figure S7. Schematic of Pipeline for Reconstruction Process, Related to Experimental Procedures

Shown is a schematic pipeline describing an abridged version of the sequence of actions and programs used in the pipeline for high-resolution reconstructions of cortical neuropil. After ATUM serial sectioning and wafer library creation, sections were multi-scale imaged at three or more different resolutions. After 3D alignment and the creation of a raw image stack, we used VAST computer assisted manual segmentation of sample volumes at high resolution to provide 'ground truth annotations' for training the Rhoanna pipeline. Rhoanna was then used to segment a new volume, cylinder 3. The results of this automatic segmentation output were then edited to correct errors by computer assisted manual correction with MOJO, in order to create a final segmentation of cylinder 3. In parallel, using VAST, we created space-filling traces of all cellular objects in cylinder 1 and cylinder 2. For cylinder 1, using VAST, we also provided annotation of all vesicles, PSDs, and mitochondria. Across expert human tracers there is < 0.5% disagreement with manual segmentation of neuronal wires using VAST and ~5% difference for counts of vesicle number. Automated segmentation (without correction by MOJO) in this dataset gave an estimated ~0.9 split operations (to correct inappropriate mergers) and 5.8 merge operations (to correct splits) per μm^3.

Cell

Supplemental Information

Saturated Reconstruction of a Volume of Neocortex

Narayanan Kasthuri, Kenneth J. Hayworth, Daniel Raimund Berger, Richard Lee Schalek, José Angel Conchello, Seymour Knowles-Barley, Dongil Lee, Amelio Vázquez-Reina, Verena Kaynig, Thouis Raymond Jones, Mike Roberts, Josh Lyskowski Morgan, Juan Carlos Tapia, H. Sebastian Seung, William Gray Roncal, Joshua Tzvi Vogelstein, Randal Burns, Daniel Lewis Sussman, Carey Eldin Priebe, Hanspeter Pfister, and Jeff William Lichtman

Supplemental Experimental Procedures

DATA ACQUISITION

Sample Preparation The sample was prepared as previously described (Tapia et al., 2012). Briefly, an anesthetized (Sodium pentobarbital, 40 mg/kg, IP) adult mouse (BALB/c) was perfused transcardially with 200 ml (flow rate ~5 ml/min) of fixative solution containing glutaraldehyde (2%; EMS, USA), p-formaldehyde (4%, EMS), CaCl2 (0.2 mM) in cacodylate buffer (0.1M, pH 7.4; EMS). The brain was removed and maintained overnight at 4°C in the same fixative solution. A 200 micron vibratome section encompassing part of the somatosensory cortex was removed and washed several times in cacodylate buffer before staining with reduced osmium tetroxide-thiocarbohydrazide (TCH)-osmium (ROTO; Tapia et al., 2012). The section was then dehydrated in alcohols, transferred to propylene oxide and immersed in 812 Epon resin (EMS, Mixture: 26 ml Epoxy resin: 15 ml DDSA: 11 ml NMA: 1 ml DMP 30). The infiltrated tissue section was cured at 60°C for two days.

Block Preparation. The cured block was trimmed using a 3 mm UltraTrim diamond knife (Diatome, USA) to a rectangle with a width to height aspect ratio of 0.6 (2 x 3 mm) and a depth of 200 μms using a ultramicrotome (UC6, Leica, Germany). The UltraTrim knife was then replaced with a 4 mm Ultra 45 diamond knife for cutting 29 nm thick serial sections.

ATUM. Automated and unattended collection of serial sections was accomplished using a custom automated tape collection device attached to a commercial ultramicrotome (ATUM). The tape collection device consists of four main components: (1) base support combined with horizontal and vertical positioning of the tape mechanism assembly, (2) tape conveyor assembly, (3) an automated syringe pump (New Era Pump Systems Model 1000, USA) and (4) software control of the tape mechanism and syringe pump. The tissue block and diamond knife were mounted in the ultramicrotome in the traditional manner. We set the goniometer and stage positions to their zero values to facilitate continuous operation. The diamond knife boat was filled with water in the standard manner. The "nose" of the tape assembly (inset, **Fig 1A**) was centered horizontally over the knife boat using the base support guide and then lowered vertically into the boat by a rack and pinion support column. The nose of the tape head was positioned in the boat at a

distance approximately 1.5 times the height of the block face (i.e., 4.5 mm) clear of the side and base panels of the boat. Using our control software, tape speed was selected to match the ultramicrotome section cutting speed of 0.3 mm/s. The water level in the knife boat changed as the tape began to move, and was readjusted to the appropriate level. A fill-spout from the syringe pump was positioned in the knife boat. Then using a video camera attached to the ultramicrotome microscope, we monitored the water level in the boat. We wrote a water level control software algorithm which measured the intensity within a box of the video frame over the meniscus at the water/knife interface showing a dark to bright gradient. When the water level drops the location in the video frame of the meniscus changes causing the syringe pump to automatically pump 20 microliters of water into the knife boat until the meniscus is restored to its original position. This process runs continuously throughout the serial sectioning run.

There are a number of potential advantages to this method of serial sectioning. Uninterrupted sectioning avoids temperature fluctuations in the microtome and tissue block that traditionally occur each time sectioning must halt to allow removal of a multi-section ribbon from a water boat. Such temperature fluctuations lead to cutting thickness variation and as a consequence, sections may shred because they are too thin or too thick. Moreover, because there is no requirement to collect as many sections as possible in a ribbon that fits within a water boat, individual serial sections can be much longer (millimeters rather than hundreds of microns), an advantage for large volume reconstruction. For the dataset described in this paper, we estimated the slice thickness was close to the ultramicrotome's set point of 29.4 nm using either the cylindrical diameter of mitochondria (Fiala and Harris, 2001) or atomic force microscopy (29.4 +/- 1 nm n=3 slices).

Because we record the cutting with a video camera we learned about knife behavior over long cutting runs and could detect exactly when failures occurred. A new diamond knife sectioning a large (>1mm) well stained block at 29 nm, missed cut somewhere between 5000 -10,000 sections. We attribute this behavior to a dulling knife-edge because when we move to a fresh part of the knife the sectioning resumes normal cutting behavior with no misses again for thousands of sections. Our impression is that strongly metal stained preparations lead to knife dulling more quickly than lighter stained blocks. With 25 nm sections, the number cut before instability is

~1000 sections. After cutting ~1000 sections, the number of attempted cuts that do not produce a section becomes ~5 per 100 sections. In general, these missing sections are not sequential. When cutting at 20 nm section thickness, we were able to collect several hundred sections before the microtome began skipping sections. In this case, the margin of error is quite small so changes in knife sharpness, temperature variations, and properties of the block all become important parameters. In spite of all of this, the missed section rate is less than 10 per 100 sections. Surprisingly, 15 nm sections did not appear much more difficult than 20 nm sections. We were able to collect 300 sections before failure at which point the missed section rate was 15 per 100 sections. Cutting 10 nm sections is difficult. The most expert microtomist in our team (RLS) has never cut more than 50 sections in a row at 10 nm. Once destabilized (after ~30 sections) the missing section rate was approximately 2-3 per 10 sections. When cutting thicker sections (29 nm), it seems that the knife sharpness is the most important parameter. As section thickness decreases, other factors become more important and recovery from missed cuts becomes more difficult.

Collection Tapes, Coatings and Processing We tried a variety of tissue collection tapes including polyamide (Kapton, Sheldahl, USA), carbon-coated Kapton, (coated by SWRI, USA), aluminum-coated Kapton (Sheldahl), conductive Kapton (Sheldahl), PEEK (Thermoplastic, USA), Lumox (Thermoplastic), polycarbonate (Thermoplastic), PET (Thermoplastic), and aluminum-coated PET (Thermoplastic). Although each of these tapes has advantages and disadvantages, we chose Kapton for this study due to its heat insensitivity and relative inelasticity.

A roll of Kapton 48 inches (1.22 m) wide, 295 ft (90 m) long and 0.002 inches (50 μms) thick was slit into strips 8 mm wide (Melton Corp., USA). The tape surface was cleaned with alcohol soaked clean room wipes. To increase its hydrophilicity we used a reel-to-reel system attached to a discharge chamber (EMS100X Glow Discharge System) and treated at an operating pressure of $1x10^{-7}$ mb, a plasma current of 50 mA and a time of 5 seconds.

Wafer Manufacture. The tape with sections attached were then transferred to four inch silicon wafers (University Wafers, USA) and attached via strips of 8 mm wide double sided carbon tape (16073, TED Pella, USA) to the polished sides of the wafers. Multiple strips were placed in parallel on each wafer (See **Figure 1**). To make the sections conductive, the wafers were then coated with ~10 nm of carbon (Edwards Auto 306 evaporator, USA).

Wafer Mapping. An automated protocol to locate and image sections on the wafers was developed (Hayworth et al., 2014 and see also Tomassy et al., 2014). For this data set a Zeiss Sigma SEM equipped with the ATLAS software (Fibics Inc., Canada) was used to both map and image the wafers. A low resolution optical image of the wafer with a digital camera allowed coarse identification of the sections on the wafer to target subsequent low and high resolution electron microscopy images.

Imaging Methods

Scanning Electron Microscopes. Four different field emission scanning electron microscopes (FESEM) were tested to acquire data: Zeiss Sigma, Zeiss Merlin, Zeiss Multi-SEM, and FEI Magellan. The Sigma was used to acquire the serial dataset described in this paper. It is the oldest scope we had access to and we had optimized its performance earliest. In terms of speed it is however the slowest at acquiring image data.

SE and BSD Imaging Modes. The serial section images were acquired using backscattered electron detection (9 kV accelerating potential, ~ 8 nA beam current, and at a working distance of ~7.3 mm). Single images using secondary electron detection were acquired using the FEI Magellan thru-the-lens detector (4 kV beam deceleration, 2 kV landing energy and beam currents ranging from 0.4 to 3.2 nA, working distance 3 mm, dwell time 25 ns). Carbon coated Kapton was required for secondary electron detection whereas the backscatter imaging was done with sections coated with carbon prior to imaging (see above). The Zeiss MultiSEM was also used to collect secondary images (landing energy of 3 kV with each scanning beam at ~560 pA, dwell time 50 nS (single beam), effective dwell time 0.8 nS per pixel for 60 beams scanning in parallel).

Image alignment and stitching. The serial section series described in this paper had relatively low amounts of distortion, in particular when compared to transmission electron microscopy

series. For the medium- and high-resolution data sets we obtained alignment by affine image transformations. Image alignment and stitching for these two data sets was done using custom Matlab scripts. The high-resolution image stack (1850 images), was aligned using a single affine transformation per image as described below.

We first computed a rigid alignment in order to initialize the affine alignment. The rigid alignment was done in two steps, first we computed pairwise relative rigid alignments between nearby pairs of images up to a certain distance. In a second step we use an iterative relaxation algorithm to bring all slices into global alignment. We use scaled-down versions of the images to speed up some of the computations, image filtering for noise reduction, regularization methods to generate low-distortion alignments, and fit-quality estimations of pairwise alignments for maximum-likelihood weighting of the relative alignments during the second step. Pairwise rigid alignment is computed using brute-force search over a set of relative image rotations in a given range, at multiple scales, computing a cross-correlation between the images for each angle.

The affine alignment is then done by using the rigid alignment to define roughly corresponding image patch locations in neighboring slices. Then, image cross-correlation is used to define accurate corresponding points of these patches on adjacent slices. Outliers are pruned from the resulting set of corresponding points and again an iterative relaxation algorithm is used to compute affine transformations which align a given image best with its neighbors, based on the available corresponding point pairs, one image at a time.

The medium-resolution image stack consisted of 255 slices, each one imaged with approximately 9x6 tiles (this varies from slice to slice). The alignment procedure was similar to the one described above, with the difference that now also the alignment to neighboring tiles also had to be taken into account. Lateral alignment of tiles in a single slice was computed using cross-correlation of the overlap regions. The final stack was aligned with one affine transformation per tile and tiles were blended where they overlapped. We then rendered aligned images for further processing. Very large images were rendered as a grid of tiles to keep the file size and image size per file limited. These methods although developed independently are similar to those described in (Saalfeld et al., 2012).

Manual Segmentation

Manual segmentation of cells and their processes was done using a custom developed volume annotation and segmentation tool (VAST; http://openconnecto.me/Kasthurietal2014/Code/VAST), a Direct3D-based Windows application. VAST allows computer-assisted manual painting of segmentation labels onto large 3D image (voxel) data sets. The aligned image stack was imported into VASTs own file format, which stored the image data in cubes, compresses it and pre-computes downsampled images for each scale, mipmaps. This data can then be viewed as 2D XY slices with interactive zooming and panning. VAST can open and dynamically load image stacks which are hosted online, from the Openconnecto.me website. In VAST painting assigns a label to individual voxels and label data is stored as a multi-resolution image stack. This differs from the reconstruction tools, trakEM2 (Cardona, et.al., 2012) and Reconstruct (Fiala, 2005), which store a vector-based representation of labels. VAST has also has options for auto-filling of contours and filling in Z to adjacent slices with the same label, which speeds up manual labeling. VAST maintains labels as a tree structure which can be edited. Each label has an ID number, color, name, anchor point (reference XYZ coordinates), tag, and location in the label hierarchy.

Both the stack of label images and the label meta-data were exported and processed further for data analysis and 3D rendering. We used Matlab scripts for data analysis and computation of surface meshes, and 3dsMax (Autodesk Inc., USA) for rendering.

Automatic Segmentation and Proofreading We developed RhoANA a processing pipeline to generate automatic segmentations, and Mojo, a proofreading and semi-automatic annotation tool. All code is open source and available online at http://openconnecto.me/Kasthurietal2014/Code/RhoANA. The processing pipeline uses methods from machine learning and computer vision to reconstruct neurons from the electron microscopy data. Human interaction is only necessary in the beginning to train a classifier for cell membrane detection by providing examples of membrane and non-membrane pixels, or by providing a small volume of fully segmented training data. The modular nature of the pipeline allows us to choose which machine learning methods to use at each stage of processing, depending on the amount of training data available and the quality of the results. Currently we use pylearn2

(Goodfellow et al., 2013b) and Maxout networks (Goodfellow et al., 2013a) to classify membranes in 2D and Fusion ((Vazquez-Reina A, 2011) (Kaynig et al., 2013)) or Gala (Nunez-Iglesias et al., 2014) to segment small 3D sub-volumes.

The automatically generated segmentations are a good first approximation of the neuron geometry, but require proofreading. For this purpose we developed Mojo and Dojo. These interfaces allow users to navigate EM images in the segmented volume with a stained glass color overlay to represent the automatic segmentation result. A range of semi-automatic tools are available to correct split or merge errors.

In order to scale to large data sets, we designed the processing pipeline to run on a computer cluster, segmenting thousands of sub-volumes in parallel. The results are then merged into one consistent segmentation.

DATA ANALYSIS

Excitatory and inhibitory synapse classification Excitatory (E) and inhibitory (I)synapses were classified according to several established criteria: 1) the presence (E) or absence of post-synaptic density staining (I) 2) whether the vesicles were large ~30-40 nm (E) or smaller (I) and 3) whether the synapse was located on a dendritic spine (E) or shaft (I) (Peters et al., 1991). If a particular synapse was ambiguous, more synapses made by the same axon were analyzed in the full high resolution volume dataset until a clear assignment could be made. Dendrites were classified as E or I by the presence or the absence of dendritic spines. Glia were classified as not receiving any synapse in the cylinder (or when traced for several microns out of the cylinder). They were also classified based on their increased tortuosity. Almost all astrocytic fragments were traced when possible to a parent cell body for further classification. After automatic segmentation in cylinder 3, each object was examined manually and classified as above.

Vesicle Annotation Vesicles were identified by evidence of their clustering in multiple sections apposed to post-synaptic densities in the case of excitatory synapses or parallel membrane lines between identified axons and dendrites in the dataset. Only vesicles with evidence of a clear synaptic center in each section were counted. Two expert tracers disagreed at 5 synapses (average vesicle no. 373) by an average of 16 vesicles. In addition, we had the same annotator re-

count vesicles at a previously counted synapse after 1 year. We found that at the same 5 synapses, the counts differed by 10 vesicles. To determine the relationship between the actual number of vesicles in a synapse and the number of vesicles counted that have a clear center in the 3 x 3 x 29 nm voxel sections we calculated the thickness of the vesicle membrane within a single section in the direction perpendicular to the section (*z*-axis in **Supplementary Figure 4**). For our calculation we assumed 40 nm vesicle diameter, 8 nm membrane thickness. We also assume that image brightness is proportional to the thickness of membrane within the section. We calculate the ratio of the brightness at the center of the vesicle to the brightest pixel. From this we obtain two curves, one for each section, of the relative brightness as a function of the depth at which the vesicle is cut. **Supplementary Figure 4** shows the result of this calculation. Only if the vesicle is cut exactly in half (extremely unlikely) would the two adjacent profiles have centers at 50% of the brightest portion of the vesicle image. Is we assume that seeing a clear center requires it be <50% the brightness of the edge then we should only count each vesicle once, meaning the counts of clear-centered vesicles are a measure of the total number of vesicles

RAMON Overview We utilized the Open Connectome Project which has developed a novel spatial database to store large-scale image and co-registered annotation datasets. The database implements the Reusable Annotation Markup for Open coNnectomics (RAMON) standard, which is a data format specification to facilitate interoperability between human and machine annotators across different research labs(Burns et al., 2013).

Searching for Orphans We defined orphan objects as one that were wholly contained in one of the cylinders. To find orphans, all the segmented objects were exported from VAST into a stack of sections with one color for each different object. We then generated two masks, a two-pixel-thick mask of the cylinder's boundary, the other of the pixels inside the cylinder. We apply these masks to each object in the VAST export. An orphan was any object that has a portion within the cylinder but not in the boundary.

Synapse reassignment (the Sudoku algorithm) To assess whether the observed number of 'redundant' synapses (defined as the number of synapses in excess of one that an axon and

dendrite ‘share’), we used Monte Carlo reassignment of the synapses among all the close contacts each axon established with dendritic spines. The inputs to the Monte Carlo procedure are one matrix containing the number of times each axon touches each dendritic spine (usually 0 or 1) and a second, corresponding matrix that contains the number of synapses each axon forms with each spine (usually 0 or 1). For the Monte Carlo simulation, we wanted to randomly generate new synaptic matrices in which 1) the number of synapses between an axon and a spine did not exceed the number of touches between that axon and spine and 2) each axon and spine participate in the same number of synapses as they do in the actual data. The synapse distribution procedure requires a list of the number of synapses each axon has available to deploy and a “touch2go” matrix which is produced by multiplying each spine column in the touch matrix by the number of synapses formed by that spine. Each iteration of network generation begins with randomly selecting one of the axons that has synapses left to deploy and retrieving the list of its available spine touches from the touch2go matrix. If touches are available, one is randomly selected for conversion to a synapse, the synapse is added to the new synapse matrix, the number of synapses available for that axon is reduced by one and the appropriate column of the touch2go matrix is reduced by one. Repetitions of this procedure can eventually lead to conflicts in which an axon has synapses left to deploy, but all of the spine touches it sees have already been consumed by other axons (i.e. an empty axon row in the touch2go matrix). This conflict is resolved by allowing the selected axon to displace another axon. A touch occupied by another axon is selected using the original touch matrix and the synapse is shifted within the new synapse matrix. The number of synapses the displaced axon has left to deploy is, therefore, increased by one. By allowing axons to steal synapses from one another, most conflicts will be resolved by local changes in connectivity, but, if necessary, these local changes can propagate to completely remodel a network and to back it out of a dead end path. The potential for biased clustering results being produced by this procedure is reduced by the fact that it is blind to the dendritic identity of each spine. In addition, we tested whether the Monte Carlo simulation had a bias towards producing synaptic matrices with too few redundant synapses by feeding it random matrices similar to our observed synaptic matrix, but without constraints on how many synapses each axon could form. Over 10k trials, we found that, on average, the random output matrix had only 0.15 more redundant synapses than the random input matrix compared to an average

absolute difference of 5.92 redundant synapses. Once each trial is completed, we sum the number of synapses each axon establishes with each dendrite and calculate the total number of redundant synapses.

Synapses on "Red" dendrite outside of cylinder Our null hypothesis is that all axons have the same probability of making additional synapses. Because the two cohorts (those that innervate spines of the red dendrite within the cylinder and those that touch spines of the red dendrite but do not innervate them in the cylinder) have the same number of axons (63) they have equal probability of making a synapse. Equivalently, a synapse has equal probability of "landing" in either cohort. That is, each synapse has 50% probability of being in each cohort. There are 12 additional synapses in the data, thus we can think of synapse assignment as flipping a coin 12 times with one cohort being heads, the other tails. The observed data has $N_1 = 11$ synapses in Cohort 1 and $N_2 = 1$ in Cohort 2. The only outcome more extreme than this is all 12 synapses in Cohort 1 ($N_1 = 12$) and none in Cohort 2. By definition, the p value is the probability of 11 synapses in Cohort 1 plus the probability of 12 synapses in Cohort 1 under the assumption that synapses are equally likely to belong to either cohort. This is, $p = \Pr\{N_1 = 11\} + \Pr\{N_1 = 12\}$. From the binomial distribution: $p = 12(1/2)^{12} + (1/2)^{12} = 13(1/2)^{12}$ which gives $p = 13/4096 \approx 0.003$

Estimate of the upper bound probability that two objects within the cylinder are the same axon To estimate the number of objects within the cylinder that are branches of other axons that pass through it we used a set of axon skeletons and a Monte Carlo simulation. In each simulation repetition, we select a random point **p** within the cylinder. From the set of axons, we randomly select one and from it we select a random segment of its skeleton and find the branch in which the segment is. The rotated cylinder is moved such that the point **p** coincides with the starting tip of the random segment. We then go through all the segments of all the other branches (the branches that do not contain the random segment) and find whether or not the branch enters the cylinder. We keep a count of the number of branches that re-enter the cylinder and calculate the mean number of re-entrant branches per axon. (We thank the anonymous reviewer who suggested this approach). To make the simulation somewhat closer to the actual data, we

discarded repetitions in which the soma of the randomly selected neuron was within the cylinder. This is because in our data there are no somata within the cylinder.

For our simulation we used NeuroMorpho neuron skeletons (Ascoli et al., 2007) provided by the laboratories of Guillermo Gonzalez-Burgos, Patrik Krieger, and Matthew F. Nolan (Garden et al., 2008; Groh et al., 2010; Yoshino et al., 2011).

We ran 40,000 repetitions of the simulation and found that the expected number of re-entrant branches per axon is $\approx 6.1\times10^{-3}$. Because there are 1308 excitatory axons in the cylinder, the expected number of re-entrant branches is ~8 (note that this is a slight overestimate because when there are re-entrant branches, the number of axons is not 1308 but some slightly smaller number).

Synapse similarity To assess the similarity of pairs of synapses made by the same axon on the same dendrite we use five metrics. Three are interval (spine volume, vesicle count, and size of the post-synaptic density), the other two dichotomous (presence or absence of mitochondria in the axon and of spine apparatus in the dendrite). For the interval metrics we assess similarity as the ratio of the larger to the smaller of the two values in each pair. From the spreadsheet in Supplementary Table 1 we select all the pairs of synapses shared by the same axon and same dendrite (SASD). We then form all possible pairs among those synapses and calculate the larger/smaller ratio for each pair. From this list, we find the SASD and non-SASD pairs. We calculate the mean ratio for each cohort and the difference of the means. We then permute the SASD/non-SASD tags among the pairs, calculate the mean ratios and their difference. We count the number of random permutations in which the difference is equal to or larger than the observed difference and obtain the p-value as this number divided by the number of permutations.

SUPPLEMENTAL REFERENCES

Cardona, A., Saalfeld, S., Schindelin, J., Arganda-Carreras, I., Preibisch, S., Longair, M., Tomancak, P., Hartenstein, V., and Douglas, R.J. (2012). TrakEM2 software for neural circuit reconstruction. PLoS ONE 7, e38011.

Fiala, J.C. (2005). Reconstruct: a free editor for serial section microscopy. J. Microsc. 218, 52–

61.

Fiala, J.C., and Harris, K.M. (2001). Cylindrical diameters method for calibrating section thickness in serial electron microscopy. J. Microsc. 202, 468–472.

Garden, D.L., Dodson, P.D., O'Donnell, C., White, M.D., and Nolan, M.F. (2008). Tuning of synaptic integration in the medial entorhinal cortex to the organization of grid cell firing fields. Neuron 60, 875–889.

Goodfellow, I.J., Warde-Farley, D., Lamblin, P., Dumoulin, V., Mirza, M., Pascanu, R., Bergstra, J., Bastien, F., and Bengio, Y. (2013a). Pylearn2: a machine learning research library. arXiv, arXiv:1308.4214, http://arxiv.org/abs/1308.4214.

Goodfellow, I.J., Warde-Farley, D., Mirza, M., Courville, A., and Bengio, Y. (2013b). Maxout networks. IMCL 28, 1319–1327.

Groh, A., Meyer, H.S., Schmidt, E.F., Heintz, N., Sakmann, B., and Krieger, P. (2010). Cell-type specific properties of pyramidal neurons in neocortex underlying a layout that is modifiable depending on the cortical area. Cereb. Cortex 20, 826–836.

Saalfeld, S., Fetter, R., Cardona, A., and Tomancak, P. (2012). Elastic volume reconstruction from series of ultra-thin microscopy sections. Nat. Methods 9, 717–720.

Yoshino, H., Miyamae, T., Hansen, G., Zambrowicz, B., Flynn, M., Pedicord, D., Blat, Y., Westphal, R.S., Zaczek, R., Lewis, D.A., and Gonzalez-Burgos, G. (2011). Postsynaptic diacylglycerol lipase mediates retrograde endocannabinoid suppression of inhibition in mouse prefrontal cortex. J. Physiol. 589, 4857–4884.